NNL04AA62G

Integration of an Autopilot for a Micro Air Vehicle

George Platanitis and Sergey Shkarayev
University of Arizona
Department of Aerospace and Mechanical Engineering, Tucson, Arizona

June 1, 2005

Table of Contents

Abstract

The following is the final report on research completed under NASA Grant NNL04AA62G, "Integration of an Autopilot for a Micro Air Vehicle." Two autopilots providing autonomous flight capabilities are presented herein. The first is the Pico-Pilot, demonstrated for the 12-inch size class of micro air vehicles. The second is the MicroPilot MP2028^{g}, where its integration into a 36-inch Zagi airframe (tailless, elevons only configuration) is investigated and is the main focus of the report.

Analytical methods, which include the use of the Advanced Aircraft Analysis software from DARCorp, were used to determine the stability and control derivatives, which were then validated through wind tunnel experiments. From the aerodynamic data, the linear, perturbed equations of motion from steady-state flight conditions may be cast in terms of these derivatives. Using these linear equations, transfer functions for the control and navigation systems were developed and feedback control laws based on Proportional, Integral, and Derivative (PID) control design were developed to control the aircraft. The PID gains may then be programmed into the autopilot software and uploaded to the microprocessor of the autopilot.

The Pico-Pilot system was flight tested and shown to be successful in navigating a 12-inch MAV through a course defined by a number of waypoints with a high degree of accuracy, and in 20 mph winds. The system, though, showed problems with control

authority in the roll and pitch motion of the aircraft, causing oscillations in these directions, but the aircraft maintained its heading while following the prescribed course.

Flight tests were performed in remote control mode to evaluate handling, adjust trim, and test data logging for the Zagi with integrated MP2028^{g}. Ground testing was performed to test GPS acquisition, data logging, and control response in autonomous mode. Technical difficulties and integration limitations with the autopilot prevented fully autonomous flight from taking place, but the integration methodologies developed for this autopilot are, in general, applicable for unmanned air vehicles within the 36-inch size class or larger that use a PID control based autopilot.

Nomenclature

AR = aspect ratio

b = wing span

c_t = wing tip chord length

c_r = wing root chord length

$C_{D\_\min}$ = zero angle-of-attack drag

C_{D1} = steady state drag

$C_{D\alpha}$ = drag coefficient derivative due to angle-of-attack

$C_{D\delta e}$ = drag coefficient derivative due to elevator deflection

C_{Lu} = lift coefficient derivative due to airspeed

C_{L1} = steady state lift

C_{Lwo} = zero angle-of-attack lift coefficient

C_{Lq} = pitch rate lift coefficient derivative

$C_{L\alpha}$ = lift coefficient derivative due to angle-of-attack

$C_{L\delta e}$ = lift coefficient derivative due to elevator deflection

C_{Mu} = moment coefficient derivative due to airspeed

C_{M1} = steady state moment coefficient

C_{Mwo} = zero angle-of-attack moment coefficient

C_{Mq} = moment coefficient derivative due to pitch rate

$C_{M\alpha}$ = moment coefficient derivative due to angle-of-attack

$C_{M\delta e}$ = moment coefficient derivative due to elevator deflection

C_{mu} = moment stability derivative due to airspeed

C_{xu} = drag stability derivative coefficient due to airspeed

$C_{x\alpha}$ = drag stability derivative coefficient due to angle-of-attack

C_{zu} = lift stability derivative due to airspeed

$C_{z\alpha}$ = lift stability derivative due to angle-of-attack

$C_{y\beta}$ = side force stability derivative coefficient due to sideslip angle

$C_{l\beta}$ = rolling moment stability derivative coefficient due to sideslip angle

C_{lp} = rolling moment stability derivative coefficient due to roll rate

C_{lr} = rolling moment stability derivative coefficient due to yaw rate

$C_{l\delta a}$ = rolling moment stability derivative coefficient due to aileron deflection

$C_{n\beta}$ = yaw moment stability derivative coefficient due to sideslip angle

C_{np} = yaw moment stability derivative coefficient due to roll rate

C_{nr} = yaw moment stability derivative coefficient due to yaw rate

$C_{n\delta a}$ = yaw moment stability derivative coefficient due to aileron deflection

$D(s)$ = Laplace transform of feedback control law

e = Oswald efficiency factor

$e(t)$ = tracking error

$E(s)$ = Laplace transform of tracking error

g = acceleration due to gravity

$G(s)$ = Laplace transform of system dynamics

h , $\dot{h}$ = altitude, rate of change of altitude

h_f = maximum fuselage height

I_{xx} = mass moment of inertia, body roll axis

I_{yy} = mass moment of inertia, body pitch axis

I_{zz} = mass moment of inertia, body yaw axis

I_{xz} = body *x*-*z* product inertia

K = proportional feedback gain

K_D = derivative feedback gain

K_I = integral feedback gain

l_f = fuselage length

m_T = total mass of aircraft, including autopilot and components

r = reference input

s = Laplace variable

S_w = wing area

T_D = derivative time

T_I = integral time

x_{ac} = aerodynamic center measured from wing apex

x_{cg} = center-of-gravity location measured from wing apex

u = perturbed airspeed

$u(t)$ = control input

U_o = steady state airspeed

$U(s)$ = Laplace transform of control input

w_f = maximum fuselage width

y = output response

α = angle-of-attack

β = sideslip angle

γ = flight path angle

δ_a = aileron deflection

δ_e = elevator deflection

θ = pitch attitude

λ = taper ratio

$\Lambda_{c/4}$ = quarter-chord wing sweep

ϕ = bank angle

ψ = heading angle

1. Introduction

Micro Air Vehicle research has been a topic of interest in recent years. In 1996, the Defense Advanced Research Projects Agency (DARPA) initiated the broad-based program on micro air vehicle research and development.[1] Applications of small, unmanned aircraft range from both military to scientific, and their versatility allows them to perform in conditions that might otherwise endanger human life, with reconnaissance capabilities being the driving factor in first generation MAVs. In several papers,[2,3,4] Micro Air Vehicle research at the University of Arizona has been presented. Here, investigations took place into the design of an adaptive wing structure, where several camber configurations (3, 6, 9, and 12 percent) of a thin, cambered plate airfoil based on the S5010-TOP24C-REF airfoil were investigated. Wind tunnel data was gathered for the lift, drag, and moment at several angles of attack over a range of freestream velocities (corresponding to associated chord Reynolds numbers). The lift-to-drag ratios were also determined and insight into optimal camber configurations were realized for various flight conditions to give best performance at both high and low flight speeds.

Flexible wing micro air vehicles have been investigated in papers by Waszak, et al.,[5] and Ifju, et al.[6] In the investigations, wing frames of varying material compositions for the wing membrane and batten arrangements of carbon fiber skeletons were constructed to provide a range of flexibilities. Their aerodynamic properties were investigated in wind tunnel experiments. The authors found that higher angles of attack may be achieved without stalling using a flexible wing that deforms under varying aerodynamic loads, including gust conditions. The deformation allows the wing to see a lower angle of

attack at higher attitudes. Also, streamlining the fuselage of the MAV improved the lift to drag ratio on the aircraft, resulting in better overall performance. Ongoing investigations in the stability and control of the MAVs are also taking place. An analysis of the static stability derivatives shows the aircraft to be stable in all axes, where the nondimensional stability derivatives were found to be generally larger than conventional, piloted aircraft.[6]

A major topic of interest in this research is in methods of developing a system for the aircraft that will allow it to fly autonomously. Several examples of previous research in micro air vehicle control may be found in Ref. 7-11. In Foster, et al.,[7] the dynamic stability of several small unmanned air vehicles (UAV) is analyzed using predictive software programs. Based on these results, handling quality guidelines are proposed using scaled-down standards normally used for larger aircraft. Thus, new short-period natural frequency standards for small UAVs may be established. In Hsiao, et al.,[8] a low cost system with an auto-lockup Charge-Coupled Device (CCD) is developed for autonomous flight and image capturing. The onboard system measures aircraft attitude, height, 3-D position via a GPS receiver, and collects data from the air data sensor and dynamic measuring unit, transmitting them to a PC-based onboard computer. An algorithm then calculates the target position for a gimbaled CCD camera, allowing real-time images to be transmitted to a ground station. Flight control is also investigated in Arning, et al.[9] The potential of using micro electromechanical systems (MEMS) technology to provide size and weight savings, along with reduced power consumption, for autopilot hardware mounted on the MAV is realized. Successful flight tests were

carried out on both fixed-wing and rotary-wing MAVs. In Taylor, et al.,[10] an attitude stabilization system based on thermal horizon detection was developed. The system operates in Visual Meteorological Conditions (VMC), is reliable in daytime or nighttime flight, consumes little power, and operates quickly from a cold start. Such a control system even allows a non-pilot the ability to fly a UAV, while giving more attention to his own projects. Finally, the ability to control MAVs is treated in Ref. 11. MEMS technology is discussed for improving MAV performance, while the rest of the paper focuses on improving airfoil design for better lift-to-drag performance. MEMS sensing and actuation may be used to delay or prevent flow separation over traditional flow control, as well as over traditional mechanical control surfaces. Also, chaotic mixing may be used to delay laminar separation. Genetic algorithms may be used in conjunction with Navier-Stokes algorithms to aid in determining an optimum profile for the design of an MAV lifting surface.

The 8th International Micro Air Vehicle Competition has showcased two designs of MAVs that demonstrated aircraft flight via an autopilot. In Ref. 12, the design team from Brigham Young University developed their aircraft through an iterative process, which involved a stability analysis of the five aircraft modes (phugoid, short period, dutch-roll, roll, and spiral), until it met functional specifications from various industry organizations. Implementation of the MAGICC autopilot provided reliable hands-off control, with capabilities that are competitive with larger UAVs, and the design was shown to be economically competitive with the most economical UAVs that are commercially available. Another entrant[13] developed a control system for autonomous flight of an

MAV for the surveillance mission of the competition. Here, an existing autopilot system was modified by the augmentation of a GPS-receiver and telemetry system which uses a waypoint navigation algorithm. Newly developed control laws were integrated into a ground station, allowing gain factors and waypoints to be modified during flight. The system developed is more flexible and the MAV can navigate pilot-independent along GPS waypoints.

At the 9th International Micro Air Vehicle Competition, a team from Konkuk University[14] made improvements in the flight ability of their MAV entry, and selected components for their MAV for surveillance and endurance missions. A micro-scale inertial measurement system, the MR01, was developed for the micro-scale autopilot system. The MR01 consists of a one-axis gyroscope sensor, and a 2-axis accelerometer. When attitude data measured by the MR01 was used as feedback for the servomotor control, longitudinal and lateral stabilities improved. Successful missions have been flown using 13-15 cm wing span MAVs for surveillance in 5 m/s headwinds.

This report focuses on the development and integration of the Pico-Pilot system for a 12-inch MAV (discussed in Sec. 2), and the integration of an autopilot system, the MP2028^{g}, for a 36-inch Zagi MAV (Sec. 4). The Pico-Pilot uses infra-red sensors to obtain information about the aircraft's attitude and orientation relative to the ground, feeding back this information to the stability system. GPS navigation is used to guide the aircraft to points along a preprogrammed flight path. The MP2028^{g} is a commercially available autopilot system that has been successfully used on large unmanned air vehicles, yet little

is known as to how feasible integration of this autopilot system is on smaller vehicles. The autopilot allows the user to program a control law onto the onboard processor, as well as mission information. The aircraft will then fly the given mission autonomously. The autopilot uses various feedback loops for navigation and control during autonomous flight. While one may use empirical approaches (set and flight test) to determine appropriate gains, the motivation of this research is to provide a more systematic approach to determining feedback loop gains. The approach involves determining an analytical model of the aircraft from its structural and aerodynamic characteristics that can then be validated through wind tunnel experiments, and developing the feedback control loops using standard design methods. Flight testing would follow to evaluate control designs. The simplest mission to evaluate autonomous capabilities of the MAV would be to have the aircraft fly to a predetermined station in an open field and then return to its point of origin. Much of the paper is devoted to the Zagi's operation, with integration of the MP2028^{g} to provide autonomous flight capabilities and developing methods to systematically determine appropriate control gains for the autopilot to provide stable flight. Finally, a section is included to summarize recent work in progress on an infra-red sensor based autopilot system under a GSA contract.

2. Pico-Pilot System for a 12-inch MAV

Results of autonomous test flights will be shown here for a 12-inch MAV design (Fig. 1). This robust aircraft served as a baseline design for the research and development program, initiated during the summer of 2004, and uses the U-NAV Pico-Pilot for the navigation system.[15]

2.1 The 12-inch Micro Air Vehicle

The airframe is constructed of vacuum molded Kevlar, making the aircraft lightweight, durable, and radio transparent. The wing is a reflexed, thin airfoil that provides good stability and performance. Conventional control surfaces (elevators and rudder) provide pitch and yaw control, and a dorsal rudder provides roll control. The brushless motor provides thrust for up to 45 degree climbs, level flight of 40 mph, and a 700 mAh rechargeable lithium battery provides power for flight durations in excess of 20 minutes.

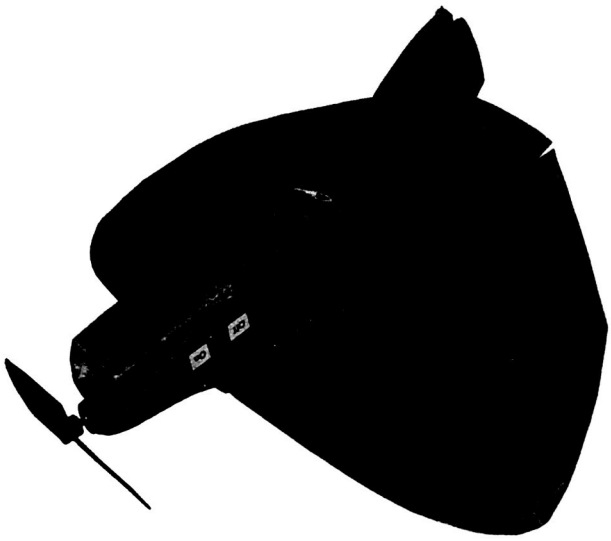

Figure 1. 12-inch MAV.

2.2 Integration of Pico-Pilot into MAV

Modifications to the 12-inch aircraft allowed it to carry a simple GPS navigation system, an optical stability system, a video camera, and sufficient battery power. The size and weight of the Pico-Pilot made it ideal because of size, weight, and price (including the

GPS receiver and antenna, the system has a mass of 56 grams and fits within the 1.5 square inch fuselage). The Pico-Pilot does not control the aircraft during take-off and landing phases and relies solely on GPS coordinate data for directional navigation. There are no software gains in the Pico-Pilot, meaning that gain adjustments have to be made through the mechanical system itself. The rudder was adjusted for a 20 deg/s yaw rate. The throttle gain could not be adjusted, but the authority it had was adequate.

The system consists of the airborne digital controller (autopilot), GPS receiver, and Waypoint Editor Software. Up to 32 waypoints can be stored in the autopilot's FLASH (non-volatile) memory. The rudder is used to handle turns, where a servo command is calculated based on the data received by the GPS receiver. A barometric pressure transducer detects altitude changes and the autopilot determines elevator or throttle commands from this data to maintain constant altitude. The attitude control loop is updated 40 times/sec, adequate for moderately stable aircraft.

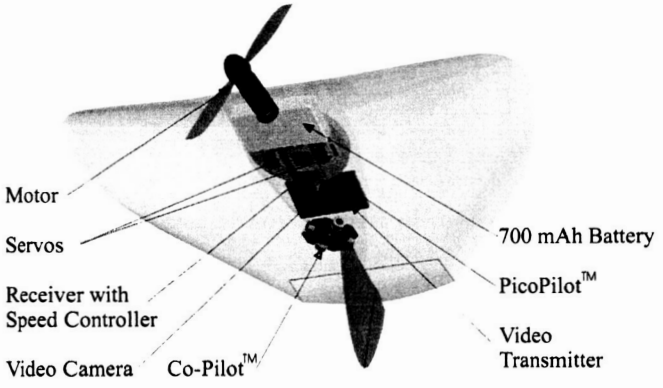

Figure 2. MAV system.

A FMA Co-Pilot system (9 grams) was integrated with the Pico-Pilot, working in parallel with the navigation system. Figure 2 depicts the arrangement of the various hardware components on the MAV. Four infra-red sensors determine the aircraft attitude relative to the ground, feeding it back to the stability system, and the elevator and dorsal rudder

are deflected as required to maintain level flight. The system prevents the aircraft from over-banking during sharp turns and can restore the aircraft to level flight from any disturbance or condition, such as inversion or stall. An 80 percent gain authority was determined to provide maximum response to the Co-Pilot without causing an overshoot. Large gains were found to cause pitch and roll oscillations, and gains too low did not provide enough authority to the Co-Pilot to keep the aircraft level.

Control loops and state tables in the autopilot manage the aircraft and navigate a mission. The heading is calculated by the flight path control loop to direct the aircraft to the next waypoint based on Track and Bearing data from the GPS receiver. The flight path control loop commands the attitude control loop to bank the aircraft at a specific angle or to adjust climb rate. The software functions are adaptive, thus calibration and setup requirements are eliminated.

2.3 Autonomous Flight Test Results

Figure 3 shows an example of a "W" course which the aircraft navigated. Such complex courses have been navigated with excellent accuracy and repeatability, with wind speeds up to 20 mph. The Co-Pilot has shown some problems with control

Figure 3. Autonomous flight way-points.

authority in the roll and pitch, causing the aircraft to oscillate in these directions. However, the aircraft still maintained its heading, following the prescribed course.

Herein, an alternative autopilot system, the MicroPilot MP2028^{g}, is investigated for the 36-inch Zagi MAV to provide autonomous flight capabilities. The size and weight of the MP2028^{g} makes it unfeasible to use in 12-inch MAVs or smaller, but the Zagi provides a useful platform to evaluate its integration into MAVs of larger sizes, comparable to the 36-inch aircraft. In additional to the capabilities of Pico-Pilot, the MicroPilot system also allows for autonomous take-off and landing.

3. Zagi MAV Background

Zagis have often been used as training aircraft for beginners in remote control flight. Commercially available Zagis (see www.zagi.com, for example)[16] are made of expanded polypropylene, a material that is resistant to damage. The aircraft may be crashed multiple times without the airframe suffering too much. As well, the "flying wing" configuration means that there are fewer parts. The Zagi MAV used for this research is a 0.926 m (36 inches) wing span (see Fig. 4), tailless aircraft configuration with physical properties described in Table 1. The wing uses a Martin Hepperle MH45 airfoil cross section, and elevons to provide control in both the longitudinal and lateral direction. Lift,

Figure 4. Views of the 36" Zagi.

drag, and moment data for the airfoil are readily available[17] and aerodynamic characteristics were calculated using methods described in Ref. 18 and 19. In the present study, the aerodynamic properties of the Zagi MAV were also validated through wind tunnel experiments.

The airframe of the 36-inch Zagi is mainly constructed of Styrofoam, with a polymer base (Kevlar) and structural reinforcement by carbon fiber rods running through the entire wing span from underneath. The control surfaces are made of balsawood and are taped to the trailing edges of the wings, with space to allow movement. They are actuated by servomotors and can deflect ±30 degrees. Plastic winglets assist in reducing

aerodynamic drag and provide some limited lateral-directional stability. A Styrofoam cap is used to protect the autopilot and associated electronics located in the "fuselage" from environmental effects and airborne particles during flight. A Rotex 25/6/15 motor with an attached propeller provides thrust. The motor is rear-mounted to eliminate aerodynamic effects due to the spinning propeller. The entire system is powered by a Polyquest PQ-B1100-HG3S lithium-polymer battery, rated at 11.1 V and 1100 mAh.

Table 1: Physical properties of Zagi MAV.

Parameter	Value	Parameter	Value
b	0.926 m	m_T	0.4309 kg
c_t	0.120 m	I_{xx}	0.02045 kg.m^2
c_r	0.2850 m	I_{yy}	0.004739 kg.m^2
λ	c_t/c_r = 0.4211	I_{zz}	0.02515 kg.m^2
S_w	0.1875 m^2	I_{xz}	2.974 x 10^{-5} kg.m^2
$\Lambda_{c/4}$	34.69°	e	0.7854
AR	4.5728	l_f	0.216 m
x_{cg} *	0.18 m	w_f	0.187 m
x_{ac} *	0.2097 m	h_f	0.052 m

*measured from aircraft nose (coincides with wing apex).

3.1 Aerodynamic Model of 36-inch Zagi

There are several methods that allow one to produce an aircraft model. One is through the use of analytical software, such as DARCorp's Advanced Aircraft Analysis (AAA), a widely used software tool by aircraft designers. Information about the software may be found at DARCorp's website (www.darcorp.com)[20]. There are ten modules in the software, including one for aerodynamic characteristics, and another for determining stability and control derivatives. At the same time, the aerodynamic data from wind tunnel experiments may be used to obtain stability and control derivatives, thus validating

computed values. In the present study, the airfoil data was utilized for the determination of the aerodynamic characteristics of the Zagi. Table 2 below summarizes the aerodynamic parameters determined using AAA software for the low flight speed range. These results provide an approximation of the flight characteristics from which a model of the aircraft can be derived.

Table 2: Aerodynamic data for the Zagi MAV.

Longitudinal		**Lateral**	
Parameter	Value	Parameter	Value
$C_{D\_\min}$	0.01631	$C_{y\beta}$	-0.07359
C_{D1}	0.02228	$C_{l\beta}$	-0.02854
$C_{D\alpha}$	0.2108	C_{lp}	-0.3209
$C_{D\delta e}$	0.3045	C_{lr}	0.03066
C_{Lu}	0.0004469	$C_{l\delta a}$	0.1682
C_{Lwo}	0.09167	$C_{n\beta}$	-0.0004012
C_{L1}	0.3964	C_{np}	-0.01297
$C_{L\alpha}$	3.5016	C_{nr}	-0.004337
C_{Lq}	2.8932	$C_{n\delta a}$	-0.003281
$C_{L\delta e}$	0.2724	$C_{M\alpha}$	-0.5675
C_{Mu}	-1.693×10^{-5}	C_{Mq}	-1.3990
C_{Mwo}	-0.02338	$C_{M\delta e}$	-0.3254
C_{M1}	-0.03489	C_{mu}	$C_{Mu}+2C_{M1}$
C_{xu}	$C_{Du}+2C_{D1}$	C_{zu}	$C_{Lu}+2C_{L1}$
$C_{x\alpha}$	$C_{D\alpha}-C_{L1}$	$C_{z\alpha}$	$C_{L\alpha}+C_{D1}$

The stability and control derivatives are determined by differentiating the force and moment equations with respect to each perturbed variable of motion (perturbed velocity, angle-of-attack, pitch rate, etc.) and the linear, perturbed equations of motion from steady-state may be cast in terms of these derivatives. These stability and control derivatives are important in efficient system design and represent the acceleration per unit

change of their associated motion or control variable. Their numerical values give an indication of their relative importance. From the linear equations of motion, six transfer functions are determined. The three longitudinal transfer functions will have an elevator input, with perturbed velocity, angle of attack, and pitch as outputs. The three lateral-directional derivatives will have an aileron input, with perturbed sideslip angle, bank angle, and heading angle as outputs. Closed-loop control laws may be designed from these transfer functions using standard control analysis.

3.2 Wind Tunnel Experiments

In order to provide validation for the use of the predicted aerodynamic data, wind tunnel measurements were made using a scaled-down model of the Zagi (at half-sized dimensions), built as a wing-only model. The actual aircraft also has a small fuselage cap to protect the autopilot hardware and electronics and its aerodynamic influence was assumed negligible. Experiments were conducted in the 4' x 3' low-speed wind tunnel at the University of Arizona. Details of the wind tunnel operation are available in Ref. 4 and 21. As only the longitudinal strain gauges were functional, only longitudinal loads could be measured. Aerodynamic data was collected for the model aircraft at a wind tunnel speed of 17.8 m/s (mean chord Reynolds number of 1.21×10^5, equivalent to the actual aircraft flying at approximately 9 m/s). At this condition, low-speed aerodynamic characteristics may be validated. The model aircraft's angle of attack and control surface deflection were varied and aerodynamic forces and moments were measured. Tares were taken for the mount and the aerodynamic influence of the mount was subtracted from the total loads measured. This way, only the loads on the aircraft remain. The 36-inch Zagi

is not expected to fly faster than ~20 m/s, a velocity range where the low-speed aerodynamic coefficients change very little.

Table 3: Experimental aerodynamic coefficients for the Zagi MAV for longitudinal forces compared against predicted values.

Parameter	Experimental Value	Predicted Value	% Error |Exp. – Pred.|/Pred.
$C_{D\_\min}$	0.02812	0.01631	72
$C_{D\alpha}$	0.07245	0.2108	66
$C_{D\delta e}$	0.009368	0.3045	97
C_{Lwo}	0.1696	0.09167	85
$C_{L\alpha}$	3.5722	3.5016	2.02
$C_{L\delta e}$	0.6238	0.2724	129

Table 3 summarizes the aerodynamic lift and drag coefficients and coefficient derivatives for angle of attack and control surface deflection, and compares them against predicted values from the AAA software. Only the coefficient derivative for lift versus angle-of-attack could be determined accurately from the experiment. The large errors between the measured and predicted values of the aerodynamic coefficients clearly show that refinements in the experimental procedure are needed. Coefficients that are generally small (such as the drag coefficients and zero angle-of-attack coefficients) will show a high level of sensitivity to measurement error, a consequence of the somewhat crude experimental setup. Also, the control surfaces are not of a typical size (~16 percent of the mean chord, whereas conventional size can be as much as 30 percent), making it difficult to measure their aerodynamic characteristics. Since the wind tunnel model aircraft did not have any means of locking the control surfaces at a desired deflection, they would experience flexibility effects caused by the dynamic pressure influence.

Despite the experimental limitations, wind tunnel studies still provide a useful tool for obtaining a model for an aircraft and validating the model against one determined by theoretical methods. Determining the aerodynamic characteristics using a wind tunnel model of an aircraft is particularly useful for aircraft that have non-conventionally shaped wings, or aircraft that are of more complex designs.

4. MP2028^g Autopilot

In the present project, the Zagi MAV is outfitted with the MP2028^g autopilot[22], designed for fully autonomous operation, from launch to recovery. Figure 5 shows how the autopilot components would be connected when integrated onto the aircraft.

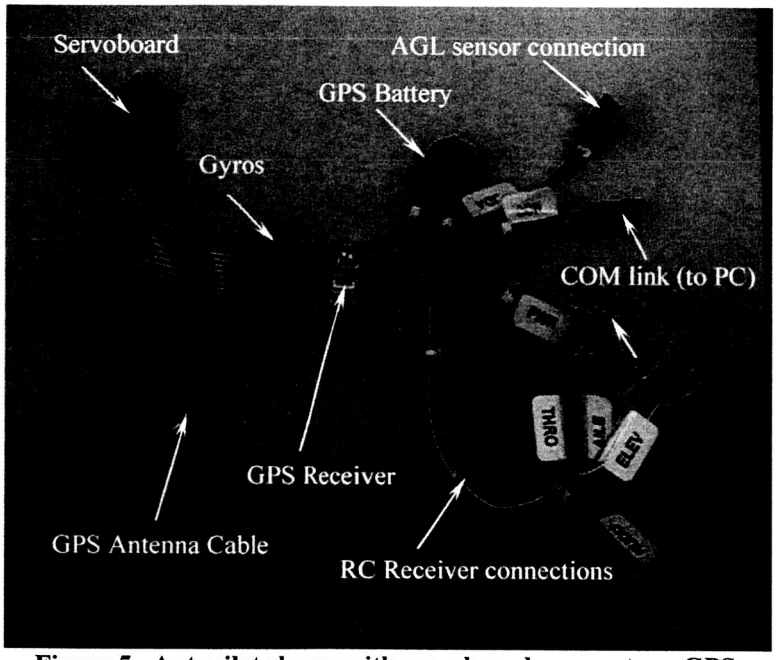

Figure 5. Autopilot shown with servoboard, connectors, GPS connector cable

4.1 Autopilot Components

The MP2028^g has a mass of 74 grams (including GPS antenna with co-axial cable and servoboard), and includes GPS navigation, airspeed hold, altitude hold, and turn coordination. The MP2028^g board itself contains the GPS receiver, microprocessor (for uploading flight and feedback control information), GPS battery, gyros, and servo and gyro sensors. The connector kit provides connectors from the autopilot to the RC receiver aileron, elevator, rudder, throttle, and Channel 5 RC select connections. Manual override is also supported, as is data logging. The GPS antenna which comes with the

autopilot is required to be set on a 3" x 3" copper plane for adequate performance. However, this configuration adds unnecessary weight (the antenna is 27.8 g, and the plate is 42.4 g), and may pose a problem for the 36-inch size class of aircraft in its flight qualities. An alternate, compatible antenna, the Sarantel 101300, was used instead because it performs equally well (both antennas were used to confirm functionality of the GPS receiver), and at 22.7 g, allows weight conservation. It is also mounted standing up and does not need a copper plane. The autopilot comes with the HORIZON^{mp} software to permit mission creation, parameter adjustment, flight monitoring, and mission simulation. Feedback loop gains and flight parameters may be programmed using the software and uploaded by the user, as well as be adjusted during flight.

Several aircraft configurations are supported by the MP2028^{g} software (flaps, flaperons, elevons, v-tail, x-tail, split rudders, split ailerons, and flap/aileron mixing), though the simulation is currently restricted to the .40 size RC trainer airframe. Other aircraft/airframe configurations would have to be tested directly in flight (during which time, control gains may be adjusted). The feedback control loops use PID control (see Appendix A). Standard control methods were implemented to determine appropriate gains for the closed-loop system to provide adequate stability and performance of the aircraft, and may be found in text books such as Ref. 23.

4.2 Hardware Integration

Figures 6 and 7 depict the autopilot and its connections with the servoboard, as well as to the RC receiver. Power is supplied to the autopilot through the P2 connector (see Fig. 6),

and power to the servoboard is direct. Separate circuit boards may be used for distributing servo signals. Up to 24 servos may be controlled by the MP2028^{g}. The servo connection shown is for a tailless, elevon only aircraft configuration. An external GPS antenna is connected to the integrated GPS receiver via a co-axial cable. An optional AGL board may be integrated into the autopilot system and provides high resolution altitude information up to 16 feet above ground; it is required for autonomous (runway) take-off and landing. The AGL board is connected to P2. Two pressure transducers measure airspeed and altitude. A Pitot tube was attached to the airspeed transducer to obtain airspeed measurements from the dynamic pressure. The altitude transducer measures altitude based on the static air pressure change with altitude change. A COM port (also connected at P2) allows the MP2028^{g} to be connected to the serial port of a PC so that the MP2028^{g} parameters can be set, as well as to download the flight datalog. The COM port is also used to connect the MP2028^{g} to a ground control station. As is also shown in Fig. 6, a remote control receiver is connected through P2, with a select through channel 5 to allow switching between autonomous and pilot-in-control mode. The MP2028^{g} settings may be changed using either of two programs: the HORIZON^{mp} ground control software (included with the MP2028^{g}), or HyperTerminal (included with Windows).

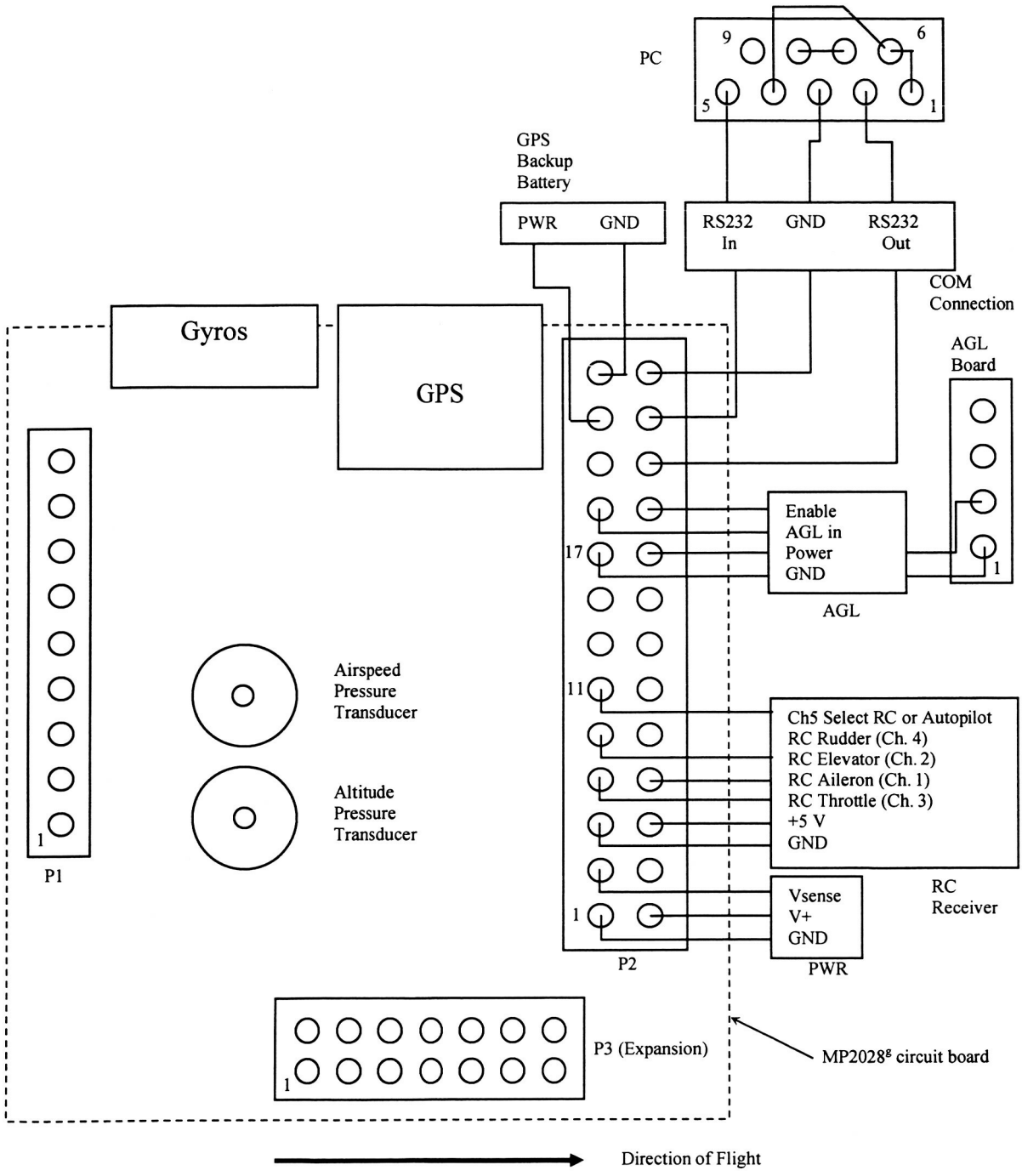

Figure 6. MP2028^g Hardware and connections.

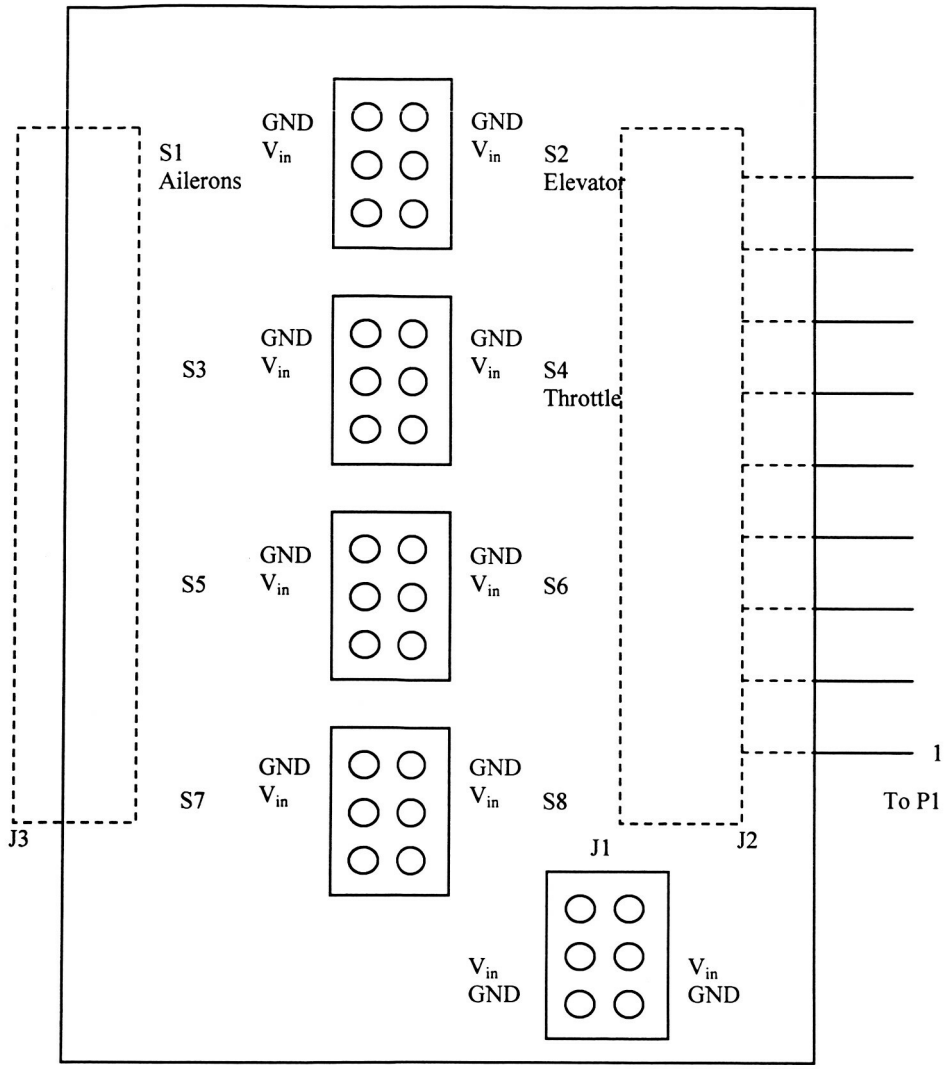

Figure 7. Servoboard connections.

The HORIZON^{mp} software is a user-friendly graphical interface, allowing the operator to create and load flight programs, adjust feedback gains, configure sensors and servos, and allow the user to interact with the aircraft during flight. HyperTerminal is useful for diagnosing and checking sensor responses after the MP2028^{g} is configured. Configuration was performed using the configuration wizard, which is included in the software package. Configuration consists of adjusting servo maximum, minimum, and zero positions, remote control transmitter response, selecting control surface types and

tail configurations (if any), checking remote control response, and obtaining a GPS lock. For the purposes of ground testing, configuration of sensors and servos, and running diagnostics on the sensor readings, the GPS lock was faked (configuration and diagnostics were mainly performed indoors). A fake GPS lock is also useful so that a user may still configure the aircraft and run diagnostics when a satellite signal is not available. The aircraft, though, must not be flown autonomously on a fake GPS lock.

5. Control Design

Several control loops are programmed into the MP2028^{g} for the purpose of maintaining stable flight and providing navigation capabilities in the autonomous flight mode. For a given airframe, the user may empirically set the PID feedback gains through flight testing, where default values of these gains are provided (located in the aircraft configuration files which can be opened in HORIZON^{mp}) as a starting point. These default values are automatically assigned during the configuration procedure. The aircraft needs to be flown autonomously with a wireless downlink to the ground station PC in order to adjust gains during flight, with gain adjustments made by observing the aircraft motion; however, a wireless link was not available at this time. However, several of the feedback loop gains may be designed more systematically if the aircraft's characteristics are known. In Table 4, the default gain values are given for the selected feedback loops[22] that PID gains will be designed for, along with a mathematical representation (Laplace transform) of their transfer functions. The full transfer functions have been defined in Appendix B. Methods for determining equations of motion of an aircraft from the stability and control derivatives, thus allowing one to obtain the transfer functions, are explained in detail in Ref. 18, 19, 23, and 24 and a control design using the derived transfer functions is shown using the elevator-from-pitch feedback loop as an example.

Table 4: Feedback Loop Gains of MP2028^g.[22]

Feedback loop	Transfer Function	Proportional Gain	Integral Gain	Derivative Gain
Aileron from Roll	$\frac{\phi(s)}{\delta_a(s)}$	-75000	-128	-3000
Elevator from Pitch	$\frac{\theta(s)}{\delta_e(s)}$	16000	9800	8900
Pitch from Altitude	$\frac{h(s)}{\theta(s)} = \frac{U_o}{s}\frac{\gamma(s)}{\theta(s)}$	320	353	800
Pitch from Airspeed	$\frac{u(s)}{\theta(s)}$	13756	24	194
Roll from Heading	$\frac{\psi(s)}{\phi(s)} = \frac{g}{U_o s}$	-200	0	-50
Pitch from Descent Rate	$\frac{\dot{h}(s)}{\theta(s)} = U_o\frac{\gamma(s)}{\theta(s)}$	-1500	-150	-1719

Table 5 shows the factors[25] needed in order to convert the gain values used by the MP2028^g to gain values that could be tested in simulation software (MATLAB®, Simulink®, etc.).[26,27] The first column is an identifier number used by the autopilot processor for that specific feedback loop. Associated with each feedback loop is a sampling rate, also given in Table 5. The sampling rate is the rate that the closed-loop system reads the input data, and must be considered (along with several factors such as rate limits, etc.) in the control design.

Table 5: Gain Conversion Factors for PID Feedback Control.[25]

	Feedback Loop		Divisor		Input units	Output units
0	Aileron From Roll (30 Hz)	P	12	4096	Radians times 1024	Fine servo
		I	15	32768		
		D	8	256	Rads per second times 1024 times 21	
1	Elevator From Pitch (30Hz)	P	9	512	Radians times 1024	Fine servo
		I	14	16384		
		D	11	2048	Rads per second times 1024 times 21	
		DD	10	1024	Rads times 1024	
6	Pitch from altitude (5Hz)	P	10	1024	Feet times 8	Radians times 1024
		I	15	32768		
		D	10	1024	Feet per second	
8	Pitch from airspeed (5Hz)	P	10	1024	Feet per second	Radians times 1024
		I	10	1024		
		D	8	256	Feet per second squared	
9	Roll from Heading (5Hz)	P	13	8192	Degrees times 100	Radians times 1024
		I	10	1024		
		D	10	1024	Degrees times 100 per second	
14	Pitch from descent rate (5Hz)	P	10	1024	Feet per second	Radians times 1024
		I	15	32768		
		D	10	1024	Feet per second squared	

Table 6: Converted Feedback Loop Gains of MP2028[g].

Feedback loop	Transfer Function	Proportional Gain	Integral Time	Derivative Time
Aileron from Roll	$\frac{\phi(s)}{\delta_a(s)}$	-0.01788	4685.99	0.03048
Elevator from Pitch	$\frac{\theta(s)}{\delta_e(s)}$	0.0305	52.214	0.0066
Pitch from Altitude	$\frac{h(s)}{\theta(s)} = \frac{U_o}{s}\frac{\gamma(s)}{\theta(s)}$	0.0119	28.993	20.0105
Pitch from Airspeed	$\frac{u(s)}{\theta(s)}$	4.0946	573.1724	0.0564
Roll from Heading	$\frac{\psi(s)}{\phi(s)} = \frac{g}{U_o s}$	-0.0140	∞	2
Pitch from Descent Rate	$\frac{\dot{h}(s)}{\theta(s)} = U_o\frac{\gamma(s)}{\theta(s)}$	-0.4465	320.0112	1.146

Each gain is split into a multiplier and a divisor to allow integer math for the autopilot to calculate the feedback loops. The gain value visible in the configuration file is a multiplier (this is the number changed when the gain is adjusted). The complete gain is the multiplier divided by the divisor. The first column of the divisor column in Table 5 is the number of bits shifted when the division is applied, and the equivalent divisor (second column) is $2^{\text{no. of bits shifted}}$. To complete the gain conversion, it is necessary to also divide by the given input units multiplying factor. As an example, the default proportional gain for the elevator-from-pitch feedback loop may be found by the following conversion,

$$K = \frac{K_{MP2028}}{Divisor * 1024} = \frac{16000}{512 * 1024} = 0.0305$$

Proceeding in a similar manner and using the definitions in Eq. A2, A4, and A6, we can convert all the gains for simulation purposes in MATLAB®. The converted gains are summarized in Table 6.

The pitch-from-elevator loop will be used as an example for designing feedback loop gains. Using the properties of Tables 1 and 2 (AAA-derived coefficients), and a flight condition of U_o = 20 m/s (steady-state velocity), with the aircraft at steady, level flight, the resulting elevator-from-pitch transfer function is the following (see Appendix B),

$$\frac{\theta(s)}{\delta_e(s)} = \frac{-13482.974s^2 - 219201.910s - 208004.227}{20s^4 + 690.171s^3 + 27641.258s^2 + 8612.602s + 30915.224} \quad (1)$$

For this transfer function, the zero-frequency gain (s = 0) is -6.7282. Consequently, a positive input to the elevon will result in a negative pitch motion, as would be expected (a downward deflection of the elevon is positive by convention). One of the easiest ways to determine gains for the PID controller is to use a root-locus plot. The root-locus plot for the elevator-from-pitch transfer function (Eq. 1) is shown in Fig. 8, with a design gain found to be suitable for a proportional feedback loop. Both positive and negative gain behaviour is shown for completion.

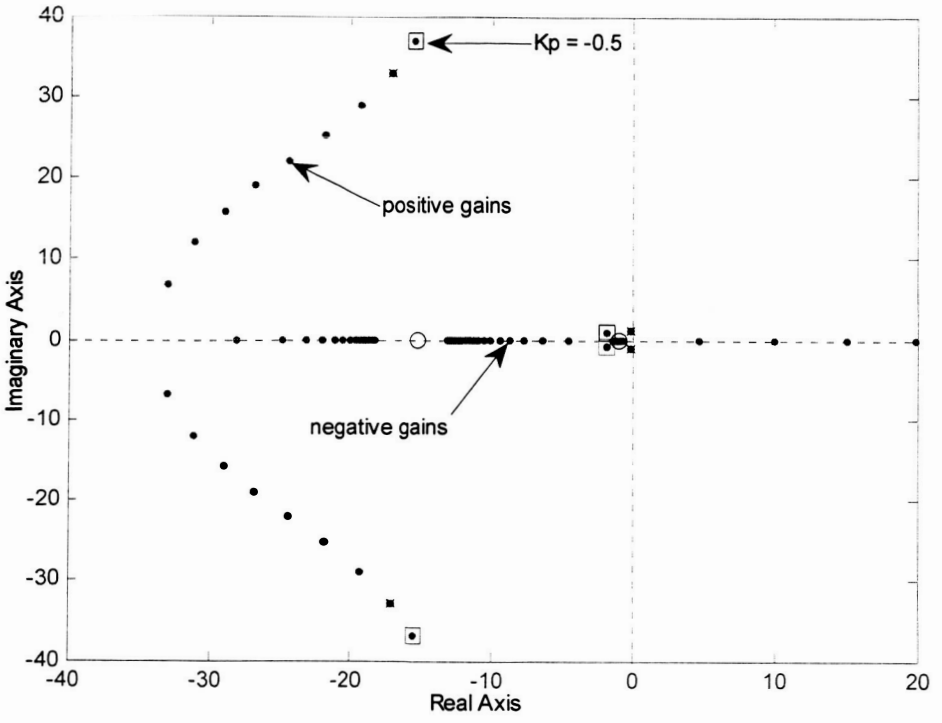

Figure 8. Root-locus plot for elevator-from-pitch.

Note how it was necessary to use a negative gain for the feedback control. This is necessary, as in the closed-loop system, a reference pitch will be read by the control law and will compare it to the response pitch. In order to produce a response pitch that will reduce the error, $e(t)$, at steady state, the control command will require the opposite sign to obtain the desired pitch. By making the gain larger and negative, the two short period poles are pushed asymptotically towards the imaginary axis, while the two phugoid poles move away from the imaginary axis within the left half plane and towards the two zeros. Note also from Table 4 that the gains were originally programmed with positive signs. When the gains are designed and converted for use in the MP2028^g, the signs will have to be changed from negative to positive. Once the proportional gain is determined, the integral and derivative terms of the control law are added (in the forward loop), and additional root-locus plots are created to determine the influence of these additional poles

and zeros (of the control law) on the closed-loop system. The integral gain, K_I (through the integral time, T_I), and derivative gain, K_D (through the derivative time, T_D), are adjusted to place the poles and zeros accordingly. Continuing with the design to produced a closed-loop system with a quick response and low steady-state errors, the following values were determined for each of the three parameters: K_P = -0.5, T_I = 1, and T_D = 0.01. Converting back to gains for use in the MP2028, the proportional, integral, and derivative gains are: K_P = 262144, K_I = 8388608, and K_D = 220201 (as they would be entered in the MP2028[g]). The root-locus plot for the PID compensated system is shown in Fig. 9.

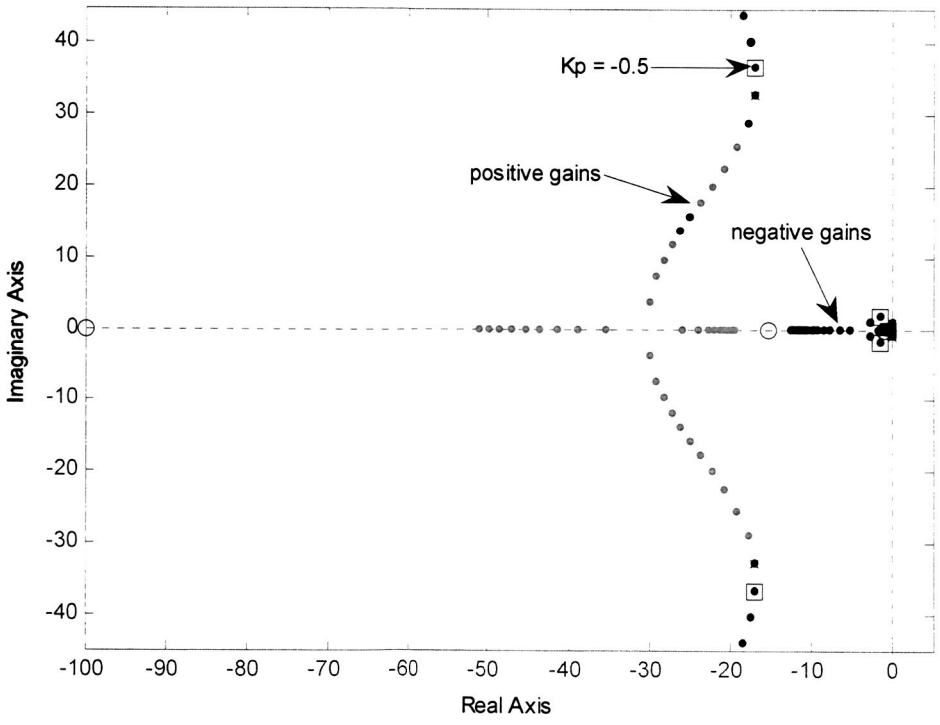

Figure 9. Root-locus plot of elevator-from-pitch with PID control in forward loop.

The PID controller used in the forward loop will add a zero at -100 from the T_D term, and an additional zero at -1 from the T_I term (and a pole at the origin). Now, as the closed-

loop system gain is increased in the negative direction, the short period poles will eventually collide near -197 on the real axis, with one pole moving to the zero at -100, and the other moving to infinity. The phugoid poles will also collide on the negative real axis, with one moving to the zero at -15.25, and the other to the zero at -1.01. The pole at the origin will move towards the zero at -1. Had a positive gain been used, the system will certainly be unstable, since the pole at the origin will move along the positive real axis. Figure 10 shows in greater detail the portion of the root-locus plot involving the phugoid poles and the pole at the origin.

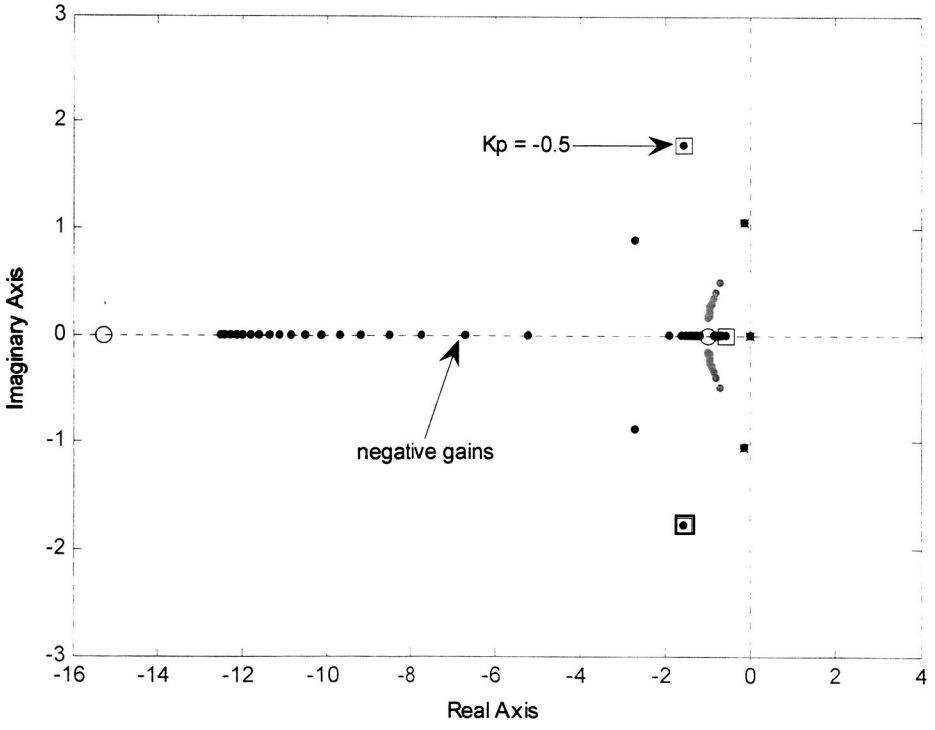

Figure 10. Magnified view of the phugoid pole behaviour.

Finally, the time response of the closed-loop system is shown in Fig. 11, simulated at a 30 Hz sampling rate (the rate used by this feedback loop). A reference pitch of 5 degrees is used here. The system responds well, settling within ~5 seconds, and exhibits a ~10 percent overshoot initially (an acceptable response).

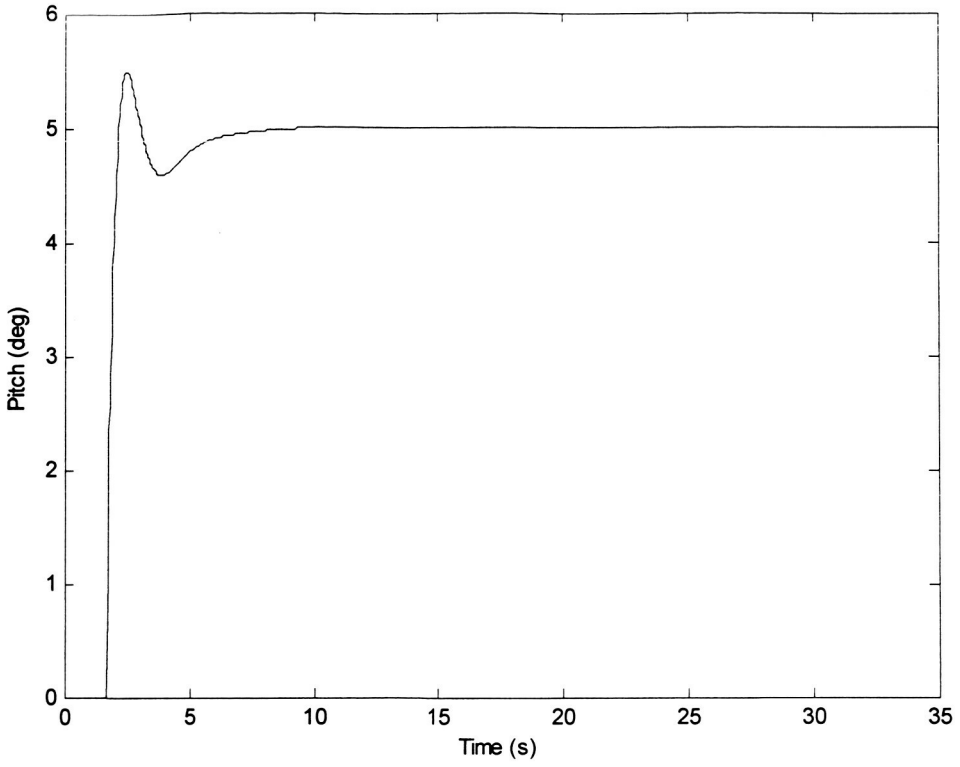

Figure 11. Response of the elevator-from-pitch closed-loop transfer function with PID compensation to a 5 degree reference pitch.

Table 7: Designed Feedback Loop Gains of MP2028[g].

Feedback loop	Proportional Gain	Integral Time	Derivative Time
Aileron from Roll	-2936	-93952	-117
Elevator from Pitch	262144	8388608	220201
Pitch from Altitude	806	1518	0
Pitch from Airspeed	4031	5039	0
Roll from Heading	-14298	0	-9
Pitch from Descent Rate	-1500	-9600	0

Using the above procedure, the PID control can be designed by simply placing the system poles appropriately through gain selection to obtain a stable, closed-loop system. The controller can then be tested to verify the time response of the system and then tuned to improve the response of the system. A relatively quick response to a step reference input is desired, while limiting the overshoot to an acceptable level. A summary of all the design gains for the various feedback loops are given in Table 7.

The feedback loops that use the pitch attitude as the "control input" are the altitude, airspeed, and descent rate loops. During level flight, the pitch attitude is used to control the aircraft altitude. For the Zagi, the following transfer function results for a 20 m/s cruise speed (see Appendix B),

$$\frac{h(s)}{\theta(s)} = \frac{580.875s^3 - 15834.059s^2 - 4423382.856s - 3628352.308}{-13482.974s^3 - 219201.910s^2 - 208004.227s} \tag{2}$$

This particular feedback loop can be controlled using a coupler (a PI control).[24] The integral gain provides a weighting factor to keep the aircraft on a desired flight path angle in the midst of disturbances (i.e., turbulence, etc.). Figure 12 shows a block diagram for an arrangement for the altitude control using pitch attitude closed-loop control system (developed from the elevator-from-pitch transfer function) in the open-loop so that the pitch response is fed directly to the pitch-from-altitude transfer function.

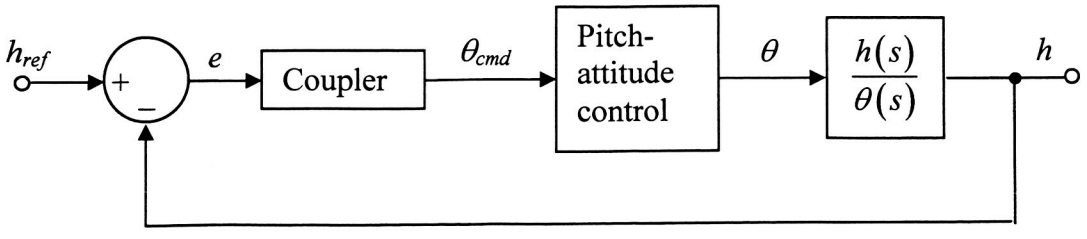

Figure 12. Altitude control using pitch closed-loop.

The pitch is used to control the descent rate as well. It is necessary to incorporate the pitch attitude control closed-loop system, derived from the elevator-from-pitch feedback loop, in the forward loop. The result is the following open-loop transfer function,

$$\frac{\dot{h}(s)}{\theta(s)} = \frac{\theta(s)}{\theta_{cmd}(s)} \cdot \frac{580.875s^3 - 15834.059s^2 - 4423382.856s - 3628352.308}{-13482.974s^2 - 219201.910s - 208004.227} \tag{3}$$

Similar to the pitch-from-altitude transfer function, a PI control may be used to control the closed-loop system.

6. Flight Testing of 36-inch Zagi with MP2028[g]

Flight tests were performed on the Zagi MAV to evaluate overall flight qualities and to test equipment functionality. Also, trim adjustments could be made during flight and response to control input, as well as external disturbances could be observed.

6.1 Remote Control Flight

A sample of the flight data for the aircraft in remote control mode is presented here. GPS functionality was not available during this set of tests. During the flight test, the aircraft was subject to large wind speeds and gusts, as well as mechanical vibrations from the motor itself. As the large amount of wind provided significant, unavoidable, external influence on the Zagi's motion, the response of the aircraft shown is not entirely due to the manual control inputs.

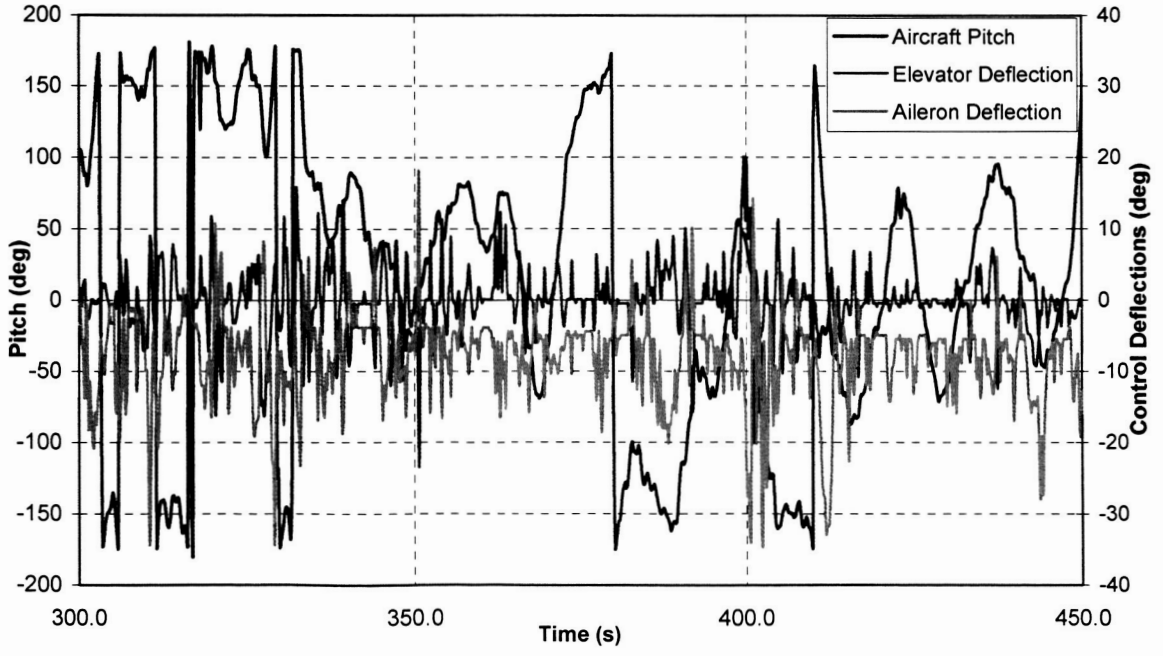

Figure 13. Pitch attitude of Zagi and control surface deflections.

Figure 13 shows the pitch angle response of the Zagi MAV to pilot inputs to the control surfaces over a small range of the flight test. The aircraft was hand launched and the motor turned on at the 300 second mark. The wind conditions made it difficult to maintain the aircraft in trim, and constant input to the control surfaces was necessary to maintain level flight. Note that where the control surface deflections are in the same direction, the control input is pure elevator. Where the control surface deflections are opposite, the deflection is pure aileron. The control surface channel connections are such that aileron deflection is the deflection of the left control surface, while the elevator deflection is the right control surface deflection.

It can be seen from Fig. 13, for example, at a time of 445 seconds, that elevator input was imparted from the remote control, causing the aircraft to pitch. During flight, trim adjustments had to be made constantly due to a slight drag and slight weight bias to the right because of equipment positioning (antenna, etc.) on the right wing (thus the negative aileron setting ~-3-6 deg). Placing the antenna out on the wing keeps the antenna isolated from the electronics at the center of the aircraft, thus minimizing interference from the rest of the electronics (this will be necessary when GPS signals are needed for autonomous flight). Some of the flight stretch shown in Fig. 13 shows normal behaviour in the pitch gyro measurement, though some cases of extreme motion are also indicated (but not actually observed during the flight). This could be due to the extreme flight conditions and motor vibrations that the gyros and sensors are being subject to, causing the gyros to "spin" and show the aircraft to be "looping", which it rarely did.

The small size of the Zagi limits the placement of the autopilot electronics, thus limiting vibration isolation for the electronic equipment and sensors.

Figure 14 shows the rolling motion of the aircraft due to the control surface deflections. Again, the biases described above caused the aircraft to roll right, therefore, constant correction was necessary to maintain level flight. In general, though, a positive aileron deflection caused the aircraft to roll in the positive direction. As with the pitch motion, some extreme motion is shown in the data, though these types of incidences, such as full rollover, were not observed as frequently during flight as the data indicates.

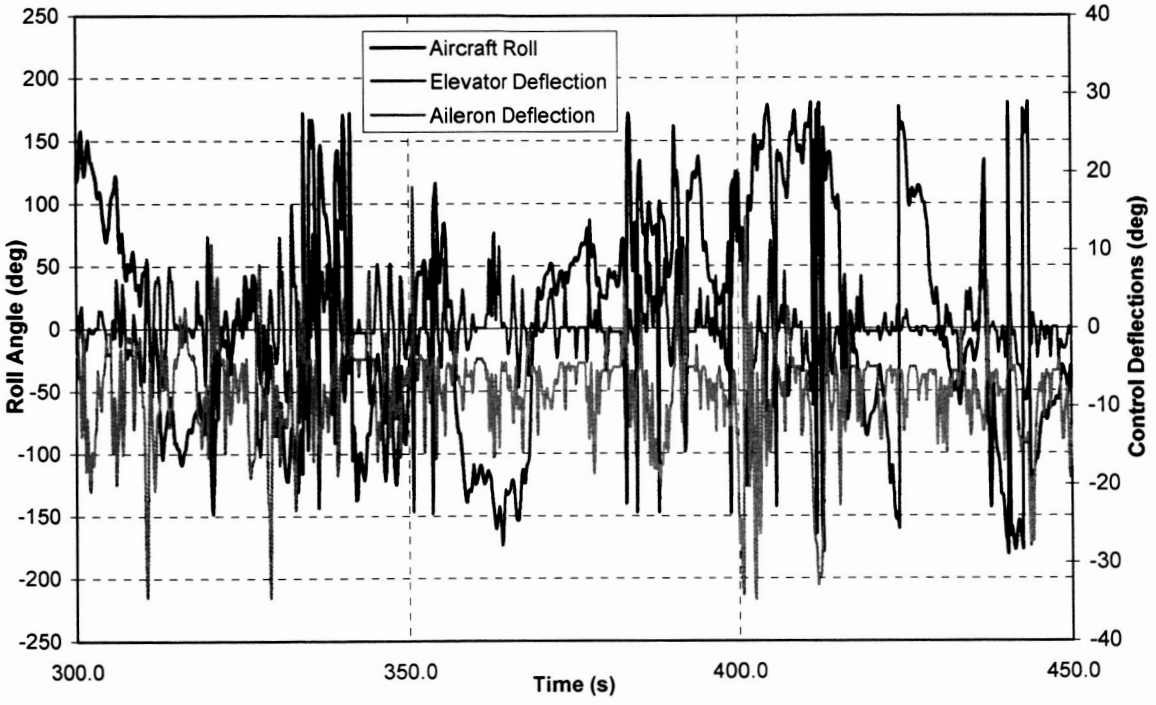

Figure 14. Rolling motion of Zagi and control surface deflections.

Finally, Fig. 15 shows the yawing motion of the aircraft due to control surfaces. Some extreme motion was recorded by the gyro sensors again (but not observed in so many instances in flight). In general, positive aileron input resulted in a positive yaw angle.

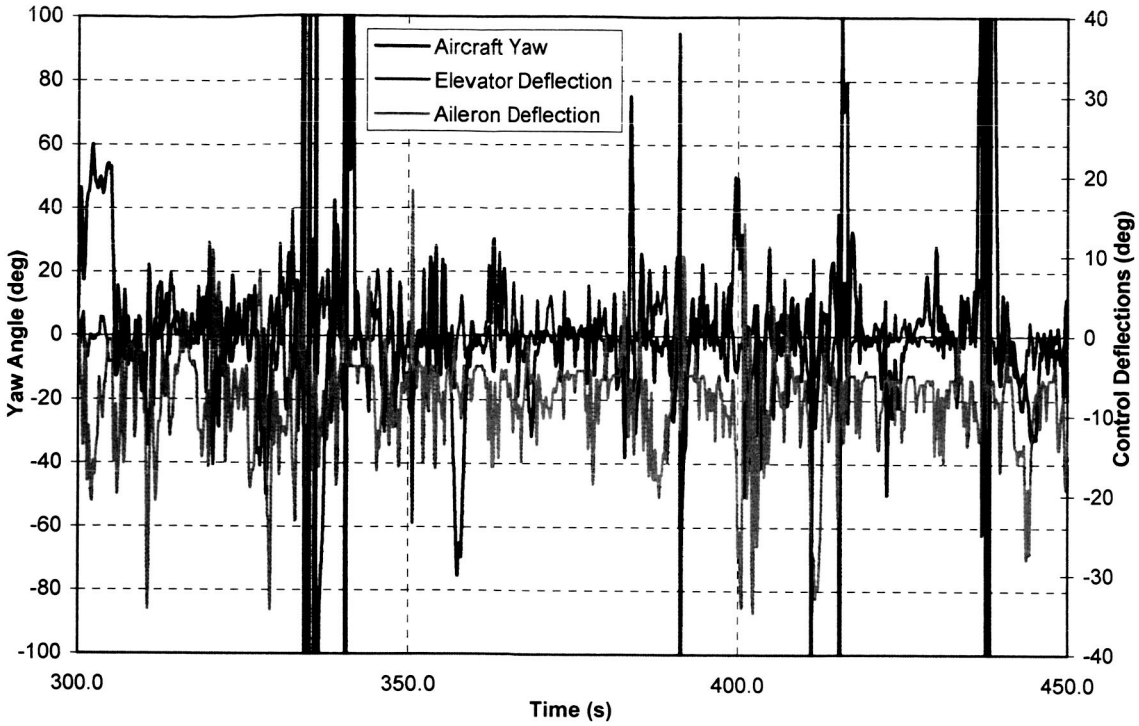

Figure 15. Yawing motion of Zagi and control surface deflections.

6.2 Ground Testing in Autonomous Mode

Figures 16-18 show ground test results with the autopilot set to autonomous mode, with results obtained when a true GPS lock was available, showing the control surface behaviour for given roll, pitch, or yaw action. While the autopilot was connected to the ground station through the COM connection, a take-off was initiated from the HORIZON^{mp} interface (the propeller was removed from the motor for safety). By hand, the aircraft was moved (to simulate disturbances) to verify control actuation. As was expected, the control surfaces moved to "oppose" the motion.

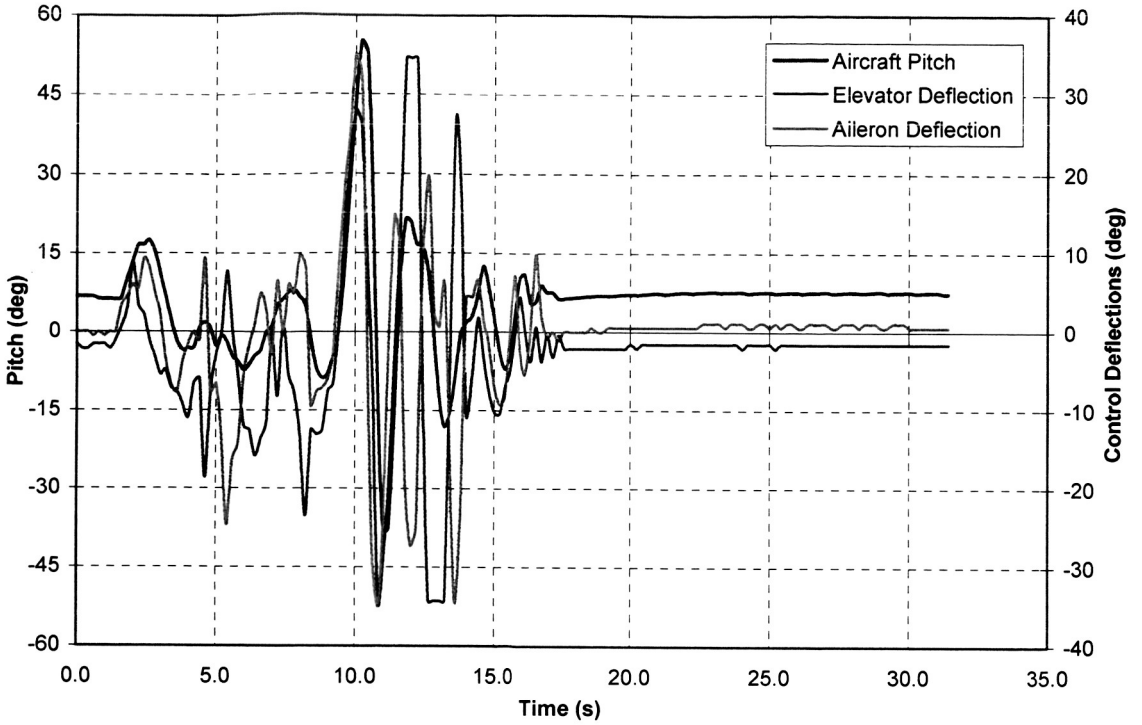

Figure 16. Control surface response to pitching motion for aircraft in autonomous mode.

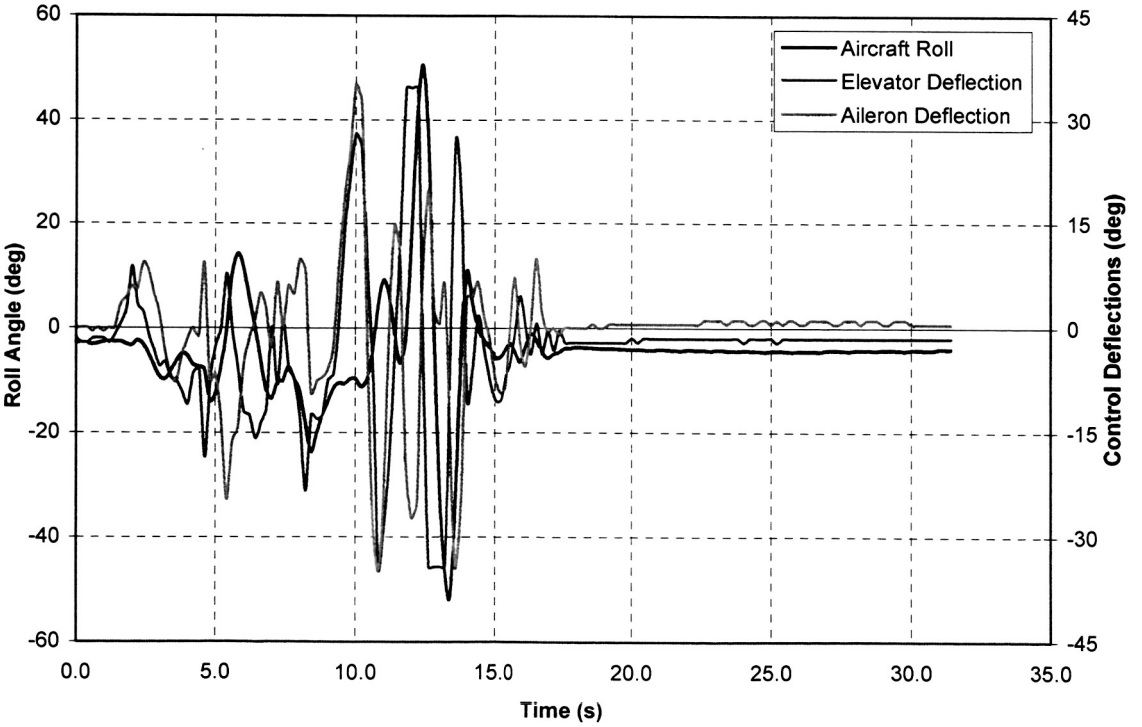

Figure 17. Control surface response to rolling motion for aircraft in autonomous mode.

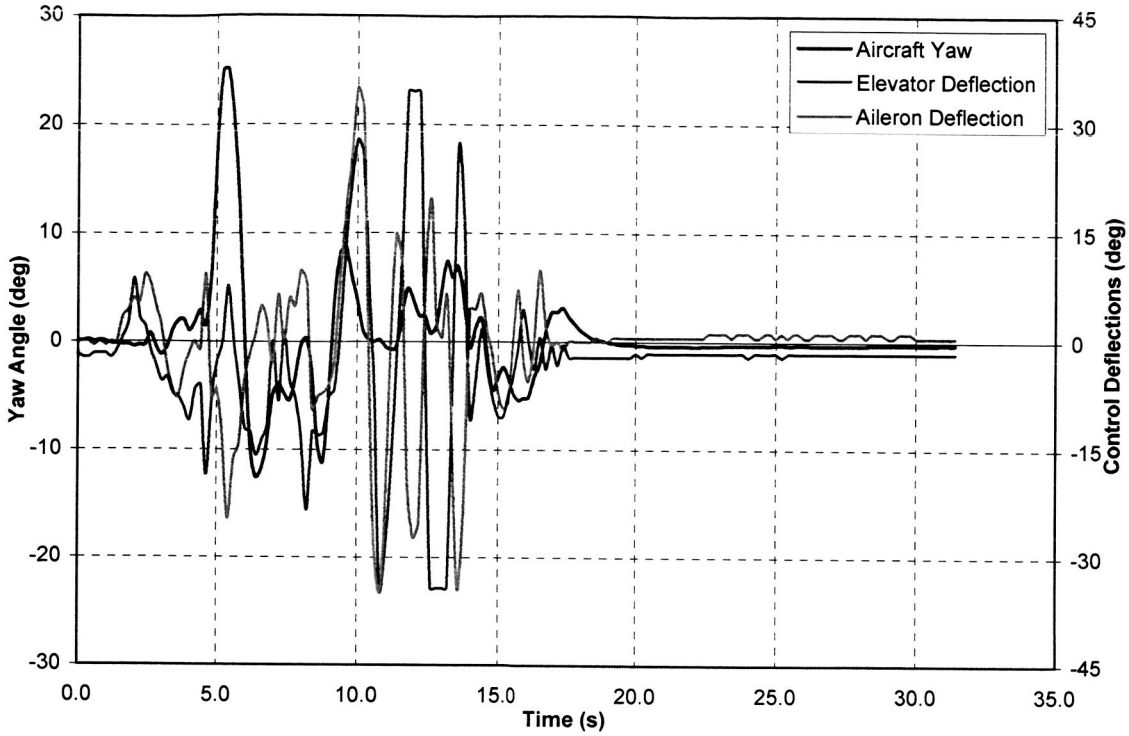

Figure 18. Control surface response to yawing motion

Since the aircraft does not have any means to directly control pure yaw disturbances (normally, that would be done by a rudder), the elevons do not deflect very much (up to ~5 degrees) to oppose pure yaw motion. Also, without a control surface to directly control heading, the autopilot has to indirectly control heading from roll, with the roll angle as an "input" (i.e., the autopilot uses the roll-from-heading feedback loop to determine the required roll, then the aileron deflection is determined using the aileron-from-roll feedback loop). If a wireless modem connection is available for the COM connection, the aircraft could be launched with assistance before a take-off command is issued, after which the aircraft should follow a predetermined flight plan when in autonomous mode.

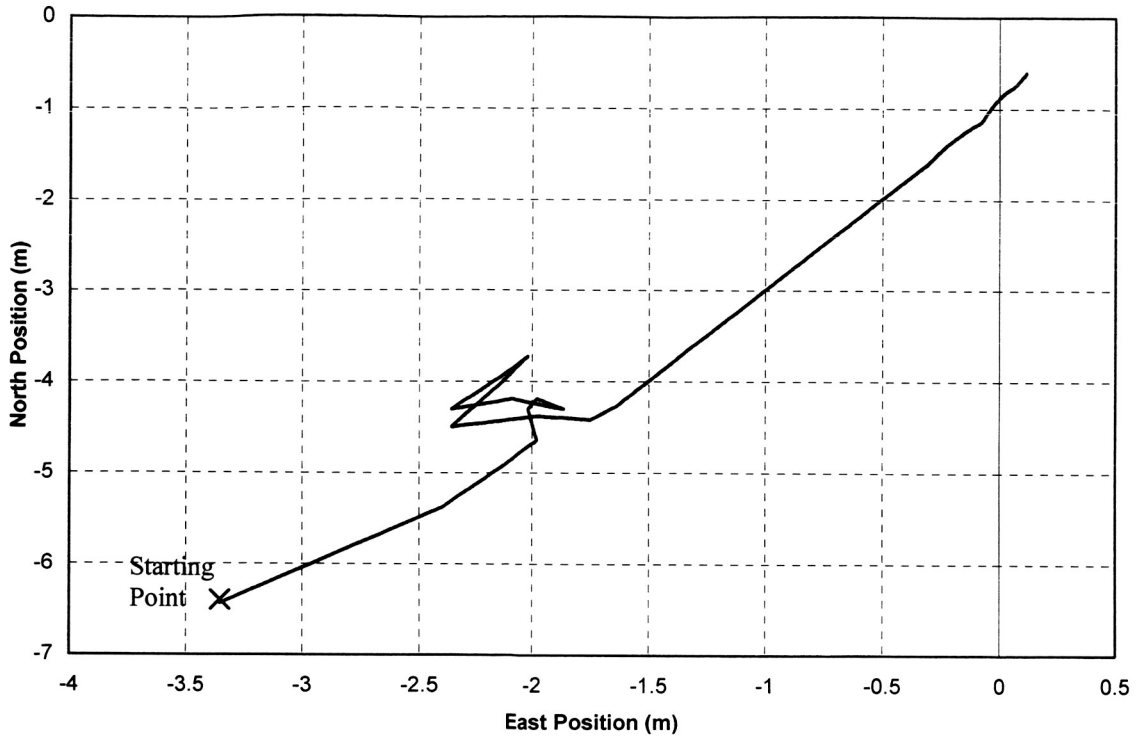

Figure 19. Position of aircraft recorded by GPS system during ground test.

Figure 19 shows ground position data that was recorded by the GPS system. During autonomous flight, the aircraft's path can be traced out and validated against the flight plan for accuracy. The starting point is offset from (0,0) by ~6.5 m South and 3.5 m West, giving an indication of the accuracy of the GPS system. As such, if a waypoint in the flight plan is located 100 m North of the starting point, its actual location could be within 6.5 m of that location along the north-south direction. GPS positioning errors will vary with availability and positioning of satellites. To help overcome uncertainties in the GPS positioning, a waypoint circle diameter can be set. This circle is what the aircraft has to enter so that the autopilot can register that a waypoint has been reached/passed.

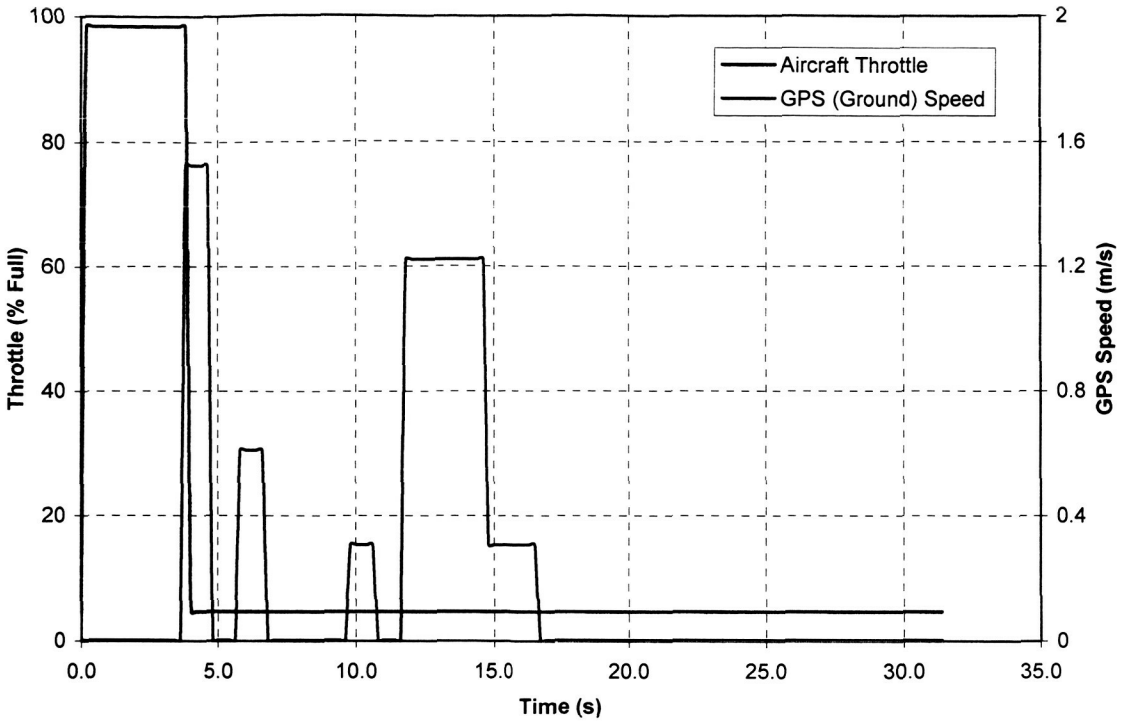

Figure 20. GPS speed and throttle during ground test in autonomous mode.

In Fig. 20, data recorded for throttle position and GPS speed (this speed is measured relative to the ground) is shown during ground testing in autonomous mode. When a take-off was initiated, the throttle briefly operated at its maximum setting, but shut off after about 4 seconds. It is expected that the throttle would continue to operate, but GPS speed was not recorded during this interval, as indicated by the plot. The autopilot did not sense that there was any motion, nor that the aircraft was actually headed to its first waypoint, and shut off the motor (which should not be the case during fully autonomous flight). After that, the GPS system sensed speed at rather sporadic intervals, suggesting that a GPS lock was not being maintained consistently (the aircraft was constantly being moved around by hand in an attempt to generate GPS speed readings).

Further ground testing was performed to determine appropriate positioning of the antenna closer to the fuselage (to avoid causing added drag from the antenna over the wing, otherwise requiring larger than normal trim adjustments in the opposite direction) and still allow the antenna to acquire a GPS signal while limiting interference between the antenna, the autopilot, and other electrical components. Interference between the antenna and the rest of the electronics may cause the antenna to acquire more slowly, not at all, or the GPS signal is more likely to be lost in flight. Due to an unexpected failure of the autopilot during a ground test over the last days of the project, autonomous flight testing could not be undertaken. During the course of the project, several failures occurred during various tests and are listed here, and action taken to overcome the problems.

Failure – inadequate RC receiver reception and range. Loss of RC reception caused autopilot to default to autonomous mode.

Action – installed dual conversion receiver to improve range; new receiver also contained a failsafe mechanism, allowing user to set a predetermined configuration of aircraft servos should RC reception be lost. Setting elevons to zero and motor off was ideal, and would allow the aircraft to glide down in the event of RC failure.

Failure – servo chatter when actuating motor or control surfaces due to larger power demand than available, as well as inadequate power distribution.

Action – original power source was 12 V, 830 mAh battery, replaced by Polyquest battery described in Sec. 3. Speed controller was also replaced to improve power distribution.

Failure – GPS receiver not responding to indicate satellite lock.

Action – Tested receiver with MicroPilot antenna with copper plane for improved response, as well as tested receiver with Sarantel antenna. Discovered that receiver was not functioning, and sent it back for replacement.

Failure – Autopilot flash chip burnt out during a ground test, possibly from a short from electrical wiring interference while testing GPS antenna positions for placement near fuselage area for better mass distribution. There is limited space around fuselage for autopilot components and wiring.

Action – Could not get a repair done because of warrantee expiration and large repair expense.

7. Infra-Red Sensor Autopilot for 12-inch MAV – Dragonfly Project

Autonomous flight research taking place parallel to the MP2028[g] integration research at the University of Arizona is the integration of an infra-red sensor autopilot[28] into a 12-inch MAV airframe, under GSA contract #9T5ZDAPS016. The autopilot under development will allow the 12-inch aircraft to fly completely autonomous through a preprogrammed flight plan of at least two waypoints, along with autonomous take-off and landing. The aircraft will be capable of at least 30 minutes of flight (with an objective endurance of 60 minutes), operate in 25 mph winds, and have a low noise and visual signature at 300 ft above ground level. The GPS waypoint navigation system is to be programmed prior to flight, allow between-flight end-user reprogramming, and be capable of landing the air vehicle at the last waypoint.

The autopilot uses infra-red sensors (non-inertial) that detect the temperature difference between the ground and sky to obtain information of the aircraft's attitude and orientation relative to the horizon. A stability-augmented system uses the temperature difference as a feedback signal to control the servos, keeping the aircraft in steady flight. The autopilot system consists of the following hardware: central processing unit (CPU), RC receiver, switching power supply, servo driver, RF link, wireless modem, GPS antenna and receiver, and the infra-red sensors. The software for the ground station is coded in C++ and can be run on a laptop running the Linux operating system. It provides a graphical interface, with modules for displaying telemetry data, configuration, mission editing and simulation, and provides a map display utility. From the ground station, missions are uploaded to the autopilot CPU.

The autopilot has been modified by researchers at the University of Arizona and a new version of the autopilot, v2, was integrated into the 12-inch aircraft and provided weight and space savings. The original two-board design was amalgamated into one circuit board. All surface mount components were placed on one side of the single board, while all connectors and large electrical components were placed on the other. The external regulator for the GPS was integrated onto the board, thus saving more weight. A couple of components were replaced with smaller counterparts in order to save on weight and size. Overall, the new design reduced the autopilot weight from 12.5 grams to 9 grams. Finally, the circuit was redesigned, and the PCB layout done. The new version of the board fits better in the 12-inch aircraft's fuselage, and its plug-and-play components make it easy to swap autopilots if necessary.

In order for the autopilot to provide proper navigation for the 12-inch aircraft, appropriate gains had to be set and algorithms coded accordingly. First, the neutrals of the horizon sensors had to be set. From this setting, the autopilot obtains information on the sensor board orientation with respect to the aircraft, and the information was hard-coded into the autopilot software. Next, the gains for roll and pitch were established to provide recovery authority. If they are set too high, the plane will oscillate; too low and the autopilot will not be able to recover from a dynamic motion. These values are again hard-coded into the autopilot.

Next, the navigation gain was established, which allows the plane to navigate between waypoints. Low gains will make the turns too wide to correct headings to waypoints; too high and turns will be overcorrected, causing roll and yaw oscillations. Again this value was programmed into the autopilot. With the navigation gain set, the maximum bank angle was then set into the autopilot, at 40 degrees. Thus, a very tight turn can be performed without altitude loss. For the navigation gain and the bank angle limit to work together, another parameter was added to the airborne code. A static elevator deflection due to bank angle was added. This "feed forward" parameter anticipates the additional elevator input needed to maintain the aircraft in a nose-up configuration upon entering a banked turn. The additional elevator input helped the aircraft maintain altitude, and tightened the turn radius. Finally the altitude gains were established. Because of the downthrust built into the design, the aircraft does not gain much altitude due to throttle. To alleviate this problem, some elevator deflection was added to the altitude loop, and hard-coded into the airborne code. The added elevator deflection improves the aircraft's altitude hold in downwind turns, and altitude changes are more accurate. At present, this value is still being adjusted to aid with decent on the landing circuit.

The 12-inch aircraft was successfully tested in the Semi-Autonomous state. The navigation gains were tuned to improve aircraft navigation such that it can navigate nearly as well as a pilot could. Take-off protocol has been written and tested with success. Landing circuits have been written with testing in progress. Altitude hold testing was first conducted to ensure the accuracy of the GPS. Accuracy as low as 3 meters AGL was shown in flight tests. Further testing of the landing circuit as well as

tuning of the altitude gains will be conducted. A fully autonomous flight, with a recoverable landing should be completed later this year.

8. Concluding Remarks

A methodology for systematically designing PID control gains for the MP2028^g autopilot was presented. First, a model of the 36-inch Zagi was developed using analytical methods, including the use of an evaluation version of the Advanced Aircraft Analysis (AAA) software available from DARCorp. The stability and control derivative coefficients were determined and compared with results from wind tunnel experiments. A scaled model of the aircraft was developed and flight conditions were replicated in wind tunnel tests by matching low speed chord Reynolds numbers. Since only the longitudinal strain gauges were functional, only the longitudinal aerodynamic loads could be measured. With the model aircraft not expected to fly faster than 20 m/s, Mach number and compressibility effects were neglected; aerodynamic characteristics remain constant for very low flight speeds. Sensitivity issues did not permit accurate measurements of many of the aerodynamic coefficients, especially those that have small values.

Using the values of the stability and control derivatives, the linear, perturbed equations of motion were formed and the six standard transfer functions were determined for both the longitudinal and lateral-directional degrees of freedom. Transfer functions were also determined from the standard transfer functions for the additional control and navigation feedback control loops that needed to be designed; in particular, altitude, airspeed, and descent rate required the addition of pitch attitude control. The MP2028^g autopilot uses proportional, integral, and derivative (PID) control. Gains were determined using root-locus analysis/pole-placement techniques. Time simulations were used to evaluate the

suitability of the chosen gains according to response speed and overshoot, and to ensure stability for the required sampling frequencies.

The 36-inch Zagi was flight tested via remote control to evaluate system functionalities, handling of the aircraft, and data gathering capabilities. At the time of these flight tests, the aircraft was subject to some extreme flight conditions, affecting the performance of the rate gyros. As revealed in the flight tests, measurements from the roll, pitch, and yaw gyros showed instances of extreme motion (looping, full rolls, and overall large angular motion) during flight, but not actually observed. As the aircraft responded quickly to control inputs and wind gusts, the gyros did not have time to settle between maneuvers or external disturbances. Also, with the motor in close proximity to the autopilot, the gyros were subject to vibrations due to the motor's operation. The small size of the Zagi limited the placement of the autopilot electronics, thus vibration isolation for the electronic equipment and sensors is limited. Ground tests of the gyros and sensors, though, under more controlled conditions did not reveal any problems. Since the feedback loops require reliable measurements from the gyros, autonomous flight with the autopilot for the 36-inch Zagi would be difficult.

Ground tests were performed with the autopilot in autonomous mode to evaluate functionality of control response and GPS data acquisition, as well as determine the approximate amount of error in GPS positioning. The aircraft showed the expected control response to oppose roll, pitch, and yaw action that may be otherwise caused by external disturbances during flight. Also, it was possible to record the aircraft's path

from the GPS positioning data. An attempt to reposition the GPS antenna closer to the fuselage instead of out on the wing was made to overcome weight distribution and drag bias; however, the drawback of the new arrangement is possible interference from the rest of the autopilot electronics, thus reducing the functionality of the antenna. Methods will need to be developed to provide isolation between the antenna and the rest of the electronics. An unexpected failure of the autopilot during the ground test prevented autonomous flight from taking place.

Flight test results were also presented for the Pico-Pilot system, an autopilot system that uses a GPS navigation system and an optical stability system. The autopilot was integrated into a 12-inch MAV and programmed to guide the aircraft through complex courses ("W" shaped, etc.). The courses were navigated with excellent accuracy and repeatability, with wind speeds up to 20 mph. There were problems with control authority in roll and pitch, with the aircraft oscillating in these directions. However, the aircraft maintained its heading as it navigated to each waypoint.

Finally, a progress summary was given on an autopilot currently under development for fully autonomous flight of a 12-inch MAV (Dragonfly). The autopilot uses infra-red sensors to detect temperature differences between the ground and the horizon. This temperature difference provides information to the autopilot as to the attitude and orientation of the aircraft relative to the horizon and the stability-augmented system uses the temperature difference to maintain the aircraft in steady flight.

References:

1. McMichael, J. M. and Francis, M.S., "Micro Air Vehicles – Toward a New Dimension in Flight," TTO document, August 7, 1997. Internet source: http://www.darpa.mil/tto/mav/mav_auvsi.html. [Cited Jan. 31st, 2005].

2. Null, W. and Shkarayev, S., "Effect of Camber on the Aerodynamics of Adaptive wing Micro Air Vehicles," *2nd AIAA Flow Control Conference*, June 28 – July 1, 2004, Portland, OR. AIAA-2004-2694.

3. Shkarayev, S., Null, W., and Wagner, M., "Development of Micro Air Vehicle Technology with In-Flight adaptive-Wing Structure," NASA/CR-2004-213271, October 2004.

4. Null, W., "The Design and Development of an Adaptive Wing Micro Air Vehicle," M.S. thesis, University of Arizona, 2003.

5. Waszak, M. R., Jenkins, L. N., and Ifju, P., "Stability and Control Properties of an Aeroelastic Fixed Wing Micro Aerial Vehicle," *AIAA Atmospheric Flight Mechanics Conference*, August 6-9, 2001, Montreal, Canada. AIAA-2001-4005.

6. Ifju, P. G., Jenkins, D. A., Ettinger, S., Lian, Y., Shyy, W., and Waszak, M. R., "Flexible-Wing-Based Micro Aerial Vehicles," *40th AIAA Aerospace Sciences Meeting and Exhibit*, January 14-17, 2002, Reno, NV. AIAA-2002-0705.

7. Foster, T. M., and Bowman, W. J., "Dynamic Stability and Handling Qualities of Small Unmanned-Aerial-Vehicles," *43rd AIAA Aerospace Sciences Meeting and Exhibit*, January 10-13, 2005, Reno, NV. AIAA-2005-1023.

8. Hsiao, F., Chien, Y., Liu, T., Lee, M., Chang, W., Han, S., and Wang, Y., "A Novel Unmanned Aerial Vehicle System with Autonomous flight and Auto-Lockup Capability," *43rd AIAA Aerospace Sciences Meeting and Exhibit*, January 10-13, 2005, Reno, NV. AIAA-2005-1050.

9. Arning, R. K. and Sassen, S., "Flight Control of Micro Aerial Vehicles," *AIAA Guidance, Navigation, and Control Conference and Exhibit*, August 16-19, 2004, Providence, RI. AIAA 2004-4911.

10. Taylor, B., Bil, C., Watkins, S., "Horizon Sensing Attitude Stabilisation: A VMC Autopilot," *18th International UAV Systems Conference*, Bristol, UK, 2003.

11. Gad-el-Hak, M., "Micro-Air-Vehicles: Can They be Controlled Better?" *Journal of Aircraft*, Vol. 38, No. 3, 2001, pp. 419-429.

12. Flake, J., Frischknecht, B., Hansen, S., Knoebel, N., Ostler, J., and Tuley, B., "Development of the Stableyes Unmanned Air Vehicle," *8th International Micro Air Vehicle Competition*, 2004, University of Arizona, Tucson, AZ.

13. Quix, H., "Design of an Autonomous Micro Air Vehicle," *8th International Micro Air Vehicle Competition*, 2004, University of Arizona, Tucson, AZ.

14. Chung, D.K., Ryu, J.H., Nam, I.C., Jo, K.Y., Yoon, K.J., Huang, H.C., and Kim, J.H., "Development of Fixed Wing MAV "Batwing" at Konkuk University," *9th International Micro Air Vehicle Competition*, 2005, Konkuk University, Seoul, South Korea.

15. *Pico-Pilot Miniature Digital Flight Control for Unmanned Air Vehicles*. User's Manual, rev 1.08.

16. Trick R/C, 2004. Internet Source: http://www.zagi.com. [Cited May 31st, 2005].

17. College of Science & Technology, Nihon University, *NASG Airfoil Database*. Internet Source: http://www.nasg.com/afdb/show-polar-e.phtml?id=441. [Cited May 31st, 2005].

18. Roskam, J., *Airplane Flight Dynamics and Automatic Flight Controls, Part I*, Design, Analysis and Research Corporation (DARCorp), 1998.

19. Roskam, J., *Methods for Estimating Stability and Control Derivatives of Conventional Subsonic Airplanes*, Roskam Aviation and Engineering Corporation, 1983.

20. Design, Analysis, and Research Corporation, 1991. Internet Source: http://www.darcorp.com. [Cited May 31st, 2005].

21. Wagner, M., "Design and Performance Analysis of a Micro Air Vehicle," M.S. thesis, University of Arizona, 2002.

22. *MicroPilot MP2028g Installation and Operation*. 2001, MicroPilot.

23. Franklin, G. F., Powel, J. D., and Emami-Naeini, A., *Feedback Control of Dynamic Systems*. Addison-Wesley Publishing Company, Inc., 1994, Third Edition.

24. Roskam, J., *Airplane Flight Dynamics and Automatic Flight Controls, Part II*, Design, Analysis and Research Corporation (DARCorp), 1998.

25. Technical correspondence with MicroPilot support staff.

26. *Control System Toolbox, User's Guide, Version 6*, The MathWorks, Inc., 2005.

27. *Simulink Control Design, Version 1*, The MathWorks, Inc., 2005.

28. Drouin, A., "PaparaDzIY – Do It Yourself UAV," Free Software Foundation, Inc., 2003. Internet Source: http://www.nongnu.org/paparazzi/index.html. [Cited May 31st, 2005].

APPENDIX A: PID Control

Since PID control will be used in the closed-loop systems for the control and navigation feedback loops of the MP2028[g], the concept of PID control will be treated briefly. The controller is a sum of the three types of control: proportional, integral, and derivative. The effect of each part on the system behaviour is presented herein.

A.1 Proportional Feedback Control

The proportional control consists of simply a gain that acts directly on the error of the measured output (i.e., the difference between the desired output and actual output). This control may be written in the general form,

$$u(t) = Ke(t) \tag{A1}$$

where $e(t)$ is the output error. Its Laplace transform would be,

$$\frac{U(s)}{E(s)} = D(s) = K \tag{A2}$$

For an aircraft, one example is the control of the aircraft pitch by an elevator deflection. Alone, a proportional control may not eliminate any steady-state offset of the system output relative to the reference input (i.e., aircraft trim), nor is it always adequate in constant disturbance rejection. Also, if the gain is too large, the stability of the system decreases. This is true especially for higher order systems. The dynamic response of the system limits how much K may be increased, thus limiting how much the steady-state error may be reduced by proportional feedback only.

A.2 Integral Feedback Control

The introduction of integral control is primarily to reduce constant steady-state errors, though the transient response may be worsened. The general form of integral feedback control is,

$$u(t) = \frac{K}{T_I} \int_{t_o}^{t} e(\tau) d\tau \tag{A3}$$

or in transfer function form,

$$\frac{U(s)}{E(s)} = D(s) = \frac{K}{T_I s} = \frac{K_I}{s} \tag{A4}$$

where T_I is the integral, or reset time, and $1/T_I$ is the reset rate, which is a measure of the speed of the response. T_I is the time required for the integrator output to reach $1 \cdot K$ for unity input. The integral control sums up all the errors of the system output since the feedback control was initiated at time t_o, allowing the integrator to reach some finite value, even if the steady-state error is zero. For an aircraft system, integral control trims the aircraft over time. An increase in the integral control gain results in lower system damping. This behaviour may be avoided by using proportional and integral control together.

A.3 Derivative Feedback Control

Derivative feedback (also called rate feedback), acts on the rate of change of the steady-state error and has the form,

$$u(t) = KT_D \dot{e}(t) \tag{A5}$$

or in transfer function form,

$$\frac{U(s)}{E(s)} = D(s) = KT_D s = K_D s \tag{A6}$$

where T_D is the derivative time. A proportional-derivative control acts in an anticipatory manner, leading the proportional-only action by T_D seconds. Derivative control is used to improve the stability of the system by increasing damping. However, alone, derivative control is not practical for many reasons. For example, if $e(t)$ is constant, then the output of the controller will be zero and a proportional or integral term would be necessary to provide the control signal.

A.4 Proportional-Integral-Derivative (PID) Feedback Control

The combination of all three control laws leads to the Proportional-Integral-Derivative feedback control and takes the following form,

$$D(s) = K\left(1 + \frac{1}{T_I s} + T_D s\right) = K + \frac{K_I}{s} + K_D s \tag{A7}$$

The PID control is widely used in various industrial processes, as well as in aircraft autopilot control design because of its effectiveness. The controller merely has to be tuned by adjusting K, T_I, and T_D. Increasing K and reducing T_I will reduce system errors, and increasing T_D tends to improve stability. Figure A1 shows how the closed-loop system with PID control may be arranged. With this arrangement, the closed loop transfer function is,

$$H(s) = \frac{G(s)}{1 + D(s)G(s)} \tag{A8}$$

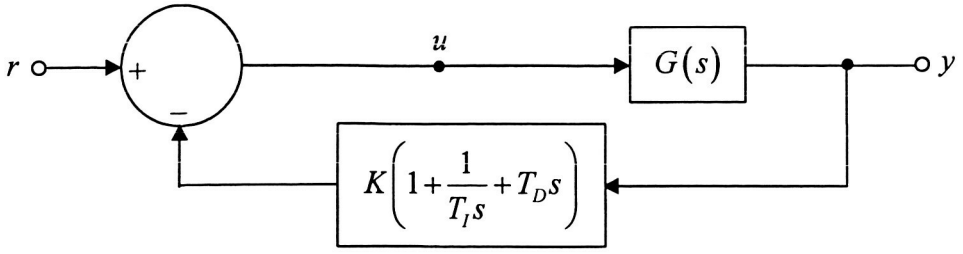

Figure A1. Closed-loop PID control.

With the control law in the feedback loop, the system response may be more desirable. In particular, with the derivative term in the feedback loop, the reference is not differentiated, which may be a favourable result. If the control law is placed in the forward loop (see Fig. A2), the derivative term will cause the system to respond faster to

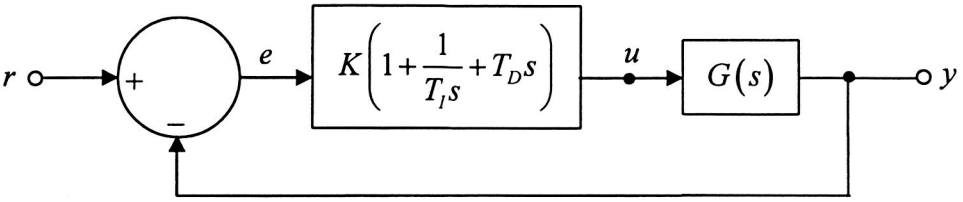

Figure A2. Alternate arrangement of closed-loop PID control.

a step reference input, but the overshoot will be higher. From the roots of the characteristic equation resulting from $1 + D(s)G(s)$, the dynamic properties of the closed-loop system may be determined. The three parameters, K, T_I, and T_D, will influence the resulting roots. Adjusting these parameters will, in theory, allow one to control the dynamics of the system.

APPENDIX B: Zagi Transfer Functions at 20 m/s Cruise Speed

Standard Longitudinal Transfer Functions:

Elevator from perturbed airspeed:

$$\frac{u(s)}{\delta_e(s)} = \frac{-649.326s^3 - 40912.976s^2 - 1010866.612s + 2149815454}{20s^4 + 690.171s^3 + 27641.258s^2 + 8612.602s + 30915.224}$$

Elevator from angle-of-attack:

$$\frac{\alpha(s)}{\delta_e(s)} = \frac{-29.044s^3 - 12691.271s^2 + 1967.233s - 26586.612}{20s^4 + 690.171s^3 + 27641.258s^2 + 8612.602s + 30915.224}$$

Elevator from pitch:

$$\frac{\theta(s)}{\delta_e(s)} = \frac{-13482.974s^2 - 219201.910s - 208004.227}{20s^4 + 690.171s^3 + 27641.258s^2 + 8612.602s + 30915.224}$$

Standard Lateral-Directional Transfer Functions:

Aileron from side-slip angle:

$$\frac{\beta(s)}{\delta_a(s)} = \frac{102.716s^3 + 8705.344s^2 + 502.750s}{20s^5 + 320.424s^4 + 175.166s^3 + 1002.624s^2 + 108.785s}$$

Aileron from roll:

$$\frac{\phi(s)}{\delta_a(s)} = \frac{7000.626s^3 + 3771.423s^2 - 10941.272s}{20s^5 + 320.424s^4 + 175.166s^3 + 1002.624s^2 + 108.785s}$$

Aileron from heading:

$$\frac{\psi(s)}{\delta_a(s)} = \frac{-102.716s^3 - 5311.834s^2 - 2068.101s - 5563.93}{20s^5 + 320.424s^4 + 175.166s^3 + 1002.624s^2 + 108.785s}$$

Other Transfer Functions:

Pitch from altitude:

$$\frac{h(s)}{\theta(s)} = \frac{U_o}{s}\frac{\gamma(s)}{\theta(s)} = \frac{U_o}{s}\left(1-\frac{\alpha(s)}{\theta(s)}\right) = \frac{U_o}{s}\left(1-\frac{\alpha(s)/\delta_e(s)}{\theta(s)/\delta_e(s)}\right), \text{ where } \gamma = \theta - \alpha$$

Pitch from perturbed airspeed:

$$\frac{u(s)}{\theta(s)} = \frac{-649.326s^3 - 40912.976s^2 - 1010866.612s + 2149815454}{-13482.974s^2 - 219201.910s - 208004.227}$$

Roll from heading:

$$\frac{\psi(s)}{\phi(s)} = \frac{g}{U_o s}$$

Pitch from descent rate:

$$\frac{\dot{h}(s)}{\theta(s)} = U_o\frac{\gamma(s)}{\theta(s)}$$